Computer Methods in Applied Mechanics and Engineering 439 (2025) 117880

Contents lists available at ScienceDirect

Comput. Methods Appl. Mech. Engrg.

journal homepage: www.elsevier.com/locate/cma

# Self-stabilized virtual element modeling of 2D mixed-mode cohesive crack propagation in isotropic elastic solids

Y. Chen [a,b,*], D. Sun [a], Q. Li [a], U. Perego [b]

[a] State Key Laboratory for Strength and Vibration of Mechanical Structures, School of Aerospace Engineering, Xi'an Jiaotong University, Xi'an 710049, China

[b] Department of Civil and Environmental Engineering, Politecnico di Milano, Milan, Italy

ARTICLE INFO

*Keywords:*
Virtual element method
Self-stabilization
Cohesive crack propagation

ABSTRACT

A comprehensive strategy for the simulation of mixed-mode cohesive crack propagation in a mesh of originally self-stabilized Virtual Elements (VEs) is proposed. Exploiting the VEs substantial insensitivity to mesh distortion, the propagating cohesive crack is accommodated within existing self-stabilized first-order quadrilateral VEs by simply adding new edges separated by a cohesive interface. The added edges make however the VE unstable and a new procedure for the stabilization of initially stable VE is developed. The method is formulated within a recently proposed Hu–Washizu variational framework, allowing for a higher order, independent modeling of stresses. In this way, a more accurate estimate of the stress at the tip of the cohesive process zone can be achieved allowing for a more accurate assessment of crack propagation conditions and direction. The proposed method is validated by application to several benchmark problems.

## 1. Introduction

One of the main difficulties involved in the Finite Element (FE) simulation of crack propagation is the treatment of the evolving displacement discontinuity in an existing FE mesh. The research literature on this topic is particularly rich. The problem has been tackled either by smearing the discontinuity, i.e. replacing the discontinuity by steep displacement gradients (see, e.g., [1,2]), or by eroding fractured elements (see, e.g., [3,4]), or by interposing interface elements along edges of existing elements (see, e.g. [5–10]), also considering polygonal meshes with a polygon splitting strategy [11], or by adopting various types of local remeshing techniques (see, e.g. [12,13]) or, finally, by suitably augmenting the finite element displacement model with discontinuous functions, as in the X-FEM (see, [14]).

The works mentioned above are only representative examples of possible approaches to the numerical modeling of crack propagation in solids and the list is by no means exhaustive. All these approaches have merits and drawbacks and may be satisfactorily employed for specific applications, which are not discussed here. In addition to these methods, the recently proposed Virtual Element Method (VEM) [15,16] allows to extend the Finite Element Method (FEM) to the use of polygonal and polyhedral elements of distorted shapes. Unlike for other methods, such as the Discontinuous-Galerkin approach, see, e.g., [8–10], where cohesive elements are preliminarily introduced at all element interfaces and where the crack is forced to propagate along directions predefined by the already existing element edges, the crack propagation direction in the VEM does not need to be pre-defined and

* Corresponding author at: State Key Laboratory for Strength and Vibration of Mechanical Structures, School of Aerospace Engineering, Xi'an Jiaotong University, Xi'an 710049, China.

*E-mail addresses:* chenyujie@stu.xjtu.edu.cn (Y. Chen), sundx96@stu.xjtu.edu.cn (D. Sun), qunli@mail.xjtu.edu.cn (Q. Li), umberto.perego@polimi.it (U. Perego).

https://doi.org/10.1016/j.cma.2025.117880
Received 19 November 2024; Received in revised form 28 January 2025; Accepted 20 February 2025

Available online 10 March 2025

cohesive elements are conveniently introduced runtime, only where needed, as dictated by the computed crack trajectory. This is possible in the VEM since it allows to define elements of arbitrary shapes without accuracy loss, enabling runtime, computationally affordable local modifications of the mesh, with the addition and/or removal of edges and nodes, or by splitting one element into two or more elements, with minimal effort. These features are ideal for incorporating a single propagating crack into an existing mesh and have been exploited by several authors proposing different applications of the VEM to the simulation of nucleation and propagation of brittle fracture [13,17–19]. Other authors also showed how the VEM can be conveniently used to compute both the Interaction Integral [20,21] and the $J_k$-Integral components [22] to assess the conditions for brittle crack propagation.

Cohesive crack propagation in a VE mesh has been considered by a limited number of authors. Artioli et al. [23] formulated a model for cohesive fracture evolution in 2D, where nucleation and propagation are driven by the max principal constant stress in a VE. Since each new crack propagation step has to cut a VE into two parts, the propagation length is dictated by the element size in the propagation direction, implying a local mesh refinement procedure to avoid overly long propagation increments. The same approach has been refined in [24], where 12-node VEs have been used. Since the crack propagation direction is taken orthogonal to the maximum principal stress direction, element stresses are first recovered based on a complementary energy minimization and then the stress field ahead of the current fictitious crack tip is smoothed using a weight function. In Choi et al. [25], a cohesive crack is allowed to propagate in a VE mesh in the direction of the mixed-mode maximum strain energy release rate, which is obtained based on the computation of the J-Integral components as domain integrals. Propagation is possible when the traction normal to the computed crack propagation direction exceeds the cohesive peak traction. Also in this case, the computation of the stress state at the fictitious cohesive crack tip is crucial and to avoid spurious oscillations in the crack path and/or in the load–displacement curve, the stress field is recovered based on a virtual grid superposed to the VE mesh.

From the literature review above, the main issues in the VEM modeling of cohesive crack propagation can be summarized as follows.

- Depending on the order of the displacement polynomial interpolation on the element edges and on the number of edges, in most cases VEs require a stabilization procedure. For a given order of polynomial interpolation along the edges, the number of zero-energy modes increases with the number of element edges. The geometric strategies implemented to accommodate the propagating crack through a VE often lead to an increased number of edges and consequent increased number of zero-energy modes.
- As in the FEM, the assessment of the conditions and direction of crack propagation requires an accurate evaluation of the stress state within the VE. In the case of brittle fracture, the J-Integral is usually computed [13,20–22], while in the case of cohesive fracture, the stress at the fictitious crack tip has to be evaluated [23–25]. Unlike in the FEM, the displacement field inside the VE is not known and its gradient cannot be used for this purpose. However, this is not a real problem since the accuracy of the displacement gradient is lower than the accuracy of displacements, and other techniques for stress recovery are normally used also in the FEM case (see, e.g. [26]). In the VEM, techniques for stress recovery, such as the superposition of a virtual grid [25], or the minimization of the complementary energy, coupled to the smoothing of the stress field by means of a weight function, as in [24], have been proposed.
- To allow a crack to propagate, a displacement discontinuity has to be introduced within the VE. Unless a smeared crack approach is pursued as, e.g., in [18], or an X-FEM enrichment of the displacement field is implemented, as in [21], a mesh modification strategy has to be devised. It may barely consist of the duplication of existing nodes, forcing in this case the crack to propagate along the direction of existing element edges [27], or of an element splitting strategy such as, e.g., in [20,22–25]. In this latter case, the almost effortless possibility to add nodes and edges to VEs and their almost complete insensitivity to distortions, open the way to inexpensive local mesh adjustments, allowing to incorporate the propagating discontinuity in the existing mesh at low computational cost.

In this work, the issues listed above are addressed for the simulation of mixed-mode cohesive crack propagation by the VEM in 2D isotropic bodies. The focus of the work is on the treatment of an evolving displacement discontinuity, due to the propagation of a cohesive crack, by the VEM rather than the accurate description of the cohesive fracture behavior of a specific material. To this purpose, the linear softening mixed-mode cohesive model proposed in [6], based on the definition of effective opening displacements and tractions, is used in the numerical applications. The model has been originally proposed for the simulation of high-speed dynamics fracture and fragmentation in brittle materials, such as rocks, aluminum, ceramics, steel [6–8,10]. Applications to concrete materials in statics have been proposed in [26], while an exponential rather than linear softening model has been considered in [7]. Although allowing for good estimates of the peak load when the correct fracture energy is employed, the linear softening model may provide less accurate results in the final stage of structural failure. In the VEM context, bilinear softening laws have been used e.g. in [24,25]. Reviews on mixed-mode cohesive zone models can be found, e.g., in [28,29].

As for the stabilization issue, the possibility of formulating self-stabilized (or, equivalently, stabilization-free) VEs has been recently considered by several authors (see, e.g., [30–36]). Self-stabilized VEs can be obtained by projecting the gradient of the unknown virtual displacement field onto a polynomial of order higher than the order of the gradient of the displacement interpolation on the element edges. As discussed in Lamperti et al. [32], this can also be interpreted as a mixed approach, emanating from a mixed Hu–Washizu variational formulation, where a modeling of the strain field is assumed independent of the displacement gradient. Besides avoiding the definition of the artificial stabilization parameter, the self-stabilized formulation provides a higher order accuracy for strains and stresses, which can be conveniently exploited for the assessment of crack propagation conditions and direction.

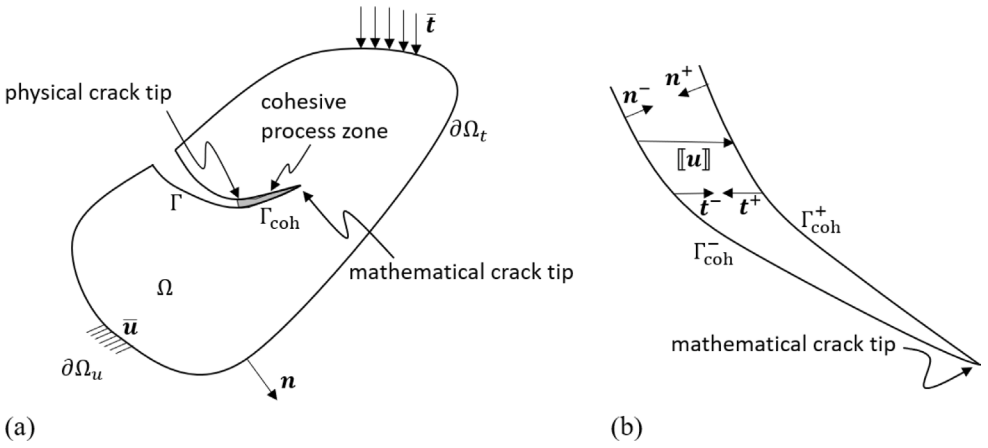


**Fig. 1.** (a) Problem definition with propagating cohesive crack. (b) Detail of cohesive process zone.

The variational Hu–Washizu mixed formulation proposed by Lamperti et al. in [32] is here enriched by the contribution of the cohesive process zone, arriving at a variationally consistent formulation of the incremental cohesive fracture problem. The problem domain is initially discretized by first-order self-stabilized quadrilateral elements with an independent linear strain model. While the stability of self-stabilized polygonal elements with an arbitrary number of edges cannot in general be rigorously established, in the special case of first-order quadrilaterals with a linear strain model, a rigorous proof of stability has been provided in [36]. The cohesive crack is allowed to propagate in the direction perpendicular to the maximum principal stress computed at the mathematical cohesive crack tip when this exceeds the critical normal cohesive traction. The assessment of this criterion requires an accurate evaluation of the stress at the current mathematical crack tip, which is obtained thanks to the adopted linear strain model together with a nodal stress smoothing procedure.

Crack propagation is achieved by an element updating and splitting strategy. Starting from the current fictitious crack tip, a crack increment $\Delta a$ is prescribed. Depending on the location of the new propagated tip, different situations may arise, which are treated separately. Exploiting the flexibility in element geometry definition offered by the VE concept, some originally quadrilateral VEs are transformed into (possibly non-convex) polygonal elements of up to 9 nodes to accommodate the propagating discontinuity. The increased number of edges creates spurious zero-energy modes in the new VE, which need be stabilized. A novel incremental stabilization technique for the originally self-stabilized VE is then developed to this purpose. Since the original VE was self-stabilized, the resulting number of spurious modes to be stabilized is always lower than in the case of the standard VEM. After the mesh updating, a cohesive interface element is introduced between the new separating edges and equilibrium of the new configuration is enforced.

The paper contents are organized as follows. The Hu–Washizu variational formulation is briefly recalled and enriched with the cohesive term in Section 2. The mixed-mode linear softening cohesive model is presented in Section 3. The FEM and VEM space discretizations of the finite-step mixed functional are discussed in Section 4. Section 5 illustrates the mesh updating strategy. The new incremental VE stabilization technique is proposed in Section 6. The implementation of the crack propagation algorithm is presented in Section 7. The numerical applications of Section 8 validate the proposed approach for the simulation of cohesive crack propagation.

For notation convenience, matrix notation is assumed for stresses $\boldsymbol{\sigma}$, strains $\boldsymbol{\varepsilon}$ and the elastic tensor $\mathbf{D}^{el}$, throughout the paper.

## 2. Cohesive-crack Hu–Washizu variational formulation

Let us consider a linear elastic isotropic and homogeneous two-dimensional body $\Omega$, with boundary $\partial\Omega = \partial\Omega_u \cup \partial\Omega_t$ with $\partial\Omega_u \cap \partial\Omega_t = \emptyset$. The body undergoes small displacements under the action of imposed displacements $\bar{\mathbf{u}}$ on $\partial\Omega_u$, prescribed tractions $\bar{\mathbf{t}}$ on $\partial\Omega_t$, and body forces $\mathbf{b}$. All the aforementioned quantities depend on a position vector $\mathbf{x}$ with respect to a Cartesian global reference system. Let $\Gamma$ denote a cohesive crack propagating under mixed-mode loading conditions, consisting of two parts: a first part terminating in the physical crack tip, where the two separating frictionless surfaces interact only when in contact; a second part, the cohesive process zone $\Gamma_{coh}$, terminating in the mathematical crack tip, where tractions normal and tangent to the surfaces are exchanged (see Fig. 1).

Let $\Gamma^+_{coh}$ and $\Gamma^-_{coh}$ denote the two faces of the cohesive crack, with normals $\mathbf{n}^+$ and $\mathbf{n}^-$, respectively. The vector $[\![\mathbf{u}]\!]$ denotes the displacement discontinuity across the crack, expressed in the global reference system, and $\mathbf{t}^+$ and $\mathbf{t}^-$ the cohesive tractions exchanged between the two sides:

$$[\![\mathbf{u}]\!] = \mathbf{u}^+ - \mathbf{u}^-, \quad \mathbf{t}^- = \mathbf{n}^-\sigma = -\mathbf{t}^+ = -\mathbf{n}^+\boldsymbol{\sigma} \tag{1}$$

where $\mathbf{n}^{\pm}$ is the matrix of director cosines of the normal to the crack faces:

$$\mathbf{n}^{\pm} = \begin{bmatrix} n_x & 0 & n_y \\ 0 & n_y & n_x \end{bmatrix}^{\pm} \tag{2}$$

Crack propagation is an irreversible process. To follow the evolution of the structural response, it is necessary to subdivide the history of loading in a sequence of finite increments and solve the propagation problem in the current time step. A sequence of time stations $t^1, \dots, t^n, t^{n+1}, \dots$ is defined, where $t^{n+1}$ is the current time and $t^n$ is the time at the end of the previous time-step. The current time increment is $\Delta t = t^{n+1} - t^n$, and the generic quantity $(\cdot)$ is discretized as $(\cdot)^{n+1} = (\cdot)^n + \Delta(\cdot)$. For brevity, the superscript $n+1$ is omitted whenever not strictly necessary, and the notation $(\cdot) := (\cdot)^{n+1}$ is adopted.

Assuming that the constitutive behavior of the cohesive interface in the considered time step is fully described by a potential function $G^n([\![\mathbf{u}]\!], \Delta D; D^n)$, where $D$ in an internal variable that can be mechanically interpreted as a damage (the used expression of $G^n$ will be presented in the next Section), the equations governing the structural response at $t^{n+1}$, i.e. at the end of the considered time step, can be obtained by enforcing the stationarity of the following extended, step-wise Hu–Washizu Lagrangian functional:

$$\begin{aligned} \Pi^n(\mathbf{u}, \boldsymbol{\varepsilon}, \boldsymbol{\sigma}, \Delta D; D^n) = & \int_{\Omega \setminus \Gamma_{coh}} \frac{1}{2} \boldsymbol{\varepsilon}^T \mathbf{D}^{el} \boldsymbol{\varepsilon} \, d\Omega - \int_{\Omega \setminus \Gamma_{coh}} \boldsymbol{\sigma}^T (\boldsymbol{\varepsilon} - \boldsymbol{\mathcal{S}}\mathbf{u}) \, d\Omega + \int_{\Gamma_{coh}} G^n([\![\mathbf{u}]\!], \Delta D; D^n) \, d\Gamma \\ & - \int_{\Omega \setminus \Gamma_{coh}} \mathbf{b}^T \mathbf{u} \, d\Omega - \int_{\partial\Omega_t} \bar{\mathbf{t}}^T \mathbf{u} \, d\partial\Omega, \quad \text{with } \Delta D \geq 0, \ \mathbf{u} = \bar{\mathbf{u}} \text{ on } \partial\Omega_u \end{aligned} \tag{3}$$

where $\boldsymbol{\mathcal{S}}$ is the small-strain compatibility operator, gathering the components of the symmetric gradient operator to be applied to the displacement field:

$$\boldsymbol{\mathcal{S}} = \begin{bmatrix} \partial_x & 0 \\ 0 & \partial_y \\ \partial_y & \partial_x \end{bmatrix} \tag{4}$$

Due to the inequality constraint on $\Delta D$ in (3), the stationarity of $\Pi^n$ is in fact a variational inequality

$$\begin{aligned} &\partial_{\mathbf{u}} \Pi^n(\mathbf{u}, \boldsymbol{\varepsilon}, \boldsymbol{\sigma}, \Delta D; D^n)[\delta\mathbf{u}] = 0, && \forall\, \delta\mathbf{u} = \mathbf{0} \text{ on } \partial\Omega_u \\ &\partial_{\boldsymbol{\varepsilon}} \Pi^n(\mathbf{u}, \boldsymbol{\varepsilon}, \boldsymbol{\sigma}, \Delta D; D^n)[\delta\boldsymbol{\varepsilon}] = 0, && \forall\, \delta\boldsymbol{\varepsilon} \\ &\partial_{\boldsymbol{\sigma}} \Pi^n(\mathbf{u}, \boldsymbol{\varepsilon}, \boldsymbol{\sigma}, \Delta D; D^n)[\delta\boldsymbol{\sigma}] = 0, && \forall\, \delta\boldsymbol{\sigma} \\ &\partial_{\Delta D} \Pi^n(\mathbf{u}, \boldsymbol{\varepsilon}, \boldsymbol{\sigma}, \Delta D; D^n)[\delta\gamma] \geq 0, && \forall\, \delta\gamma = \Delta D' - \Delta D, \text{ with } \Delta D' \geq 0, \ \Delta D \geq 0, \end{aligned} \tag{5}$$

where $\Delta D'$ is an arbitrary non-negative field defined on $\Gamma_{coh}$. The inequality in the variational system (5) can be rewritten in complementarity form, obtaining the equilibrium equations, the linear elastic stress–strain relation, the compatibility condition and the damage activation conditions in the usual Kuhn–Tucker form:

$$\begin{aligned} &\partial_{\mathbf{u}} \Pi^n[\delta\mathbf{u}] = 0 \Rightarrow \int_{\Omega \setminus \Gamma_{coh}} [(\boldsymbol{\mathcal{S}}^T \boldsymbol{\sigma}) + \mathbf{b}]^T \delta\mathbf{u} \, d\Omega + \int_{\partial\Omega_t} \bar{\mathbf{t}}^T \delta\mathbf{u} \, d\partial\Omega \\ &\qquad + \int_{\Gamma_{coh}} (\mathbf{t}^+)^T \delta\mathbf{u}^+ \, d\Gamma + \int_{\Gamma_{coh}} (\mathbf{t}^-)^T \delta\mathbf{u}^- \, d\Gamma = 0 \quad \forall\, \delta\mathbf{u} = \mathbf{0} \text{ on } \partial\Omega_u, \\ &\partial_{\boldsymbol{\varepsilon}} \Pi^n[\delta\boldsymbol{\varepsilon}] = 0 \Rightarrow \int_{\Omega \setminus \Gamma_{coh}} (\mathbf{D}^{el} \boldsymbol{\varepsilon} - \boldsymbol{\sigma})^T \delta\boldsymbol{\varepsilon} \, d\Omega = 0 \quad \forall\, \delta\boldsymbol{\varepsilon}, \\ &\partial_{\boldsymbol{\sigma}} \Pi^n[\delta\boldsymbol{\sigma}] = 0 \Rightarrow \int_{\Omega \setminus \Gamma_{coh}} (\boldsymbol{\varepsilon} - \boldsymbol{\mathcal{S}}\mathbf{u})^T \delta\boldsymbol{\sigma} \, d\Omega = 0 \quad \forall\, \delta\boldsymbol{\sigma}, \\ &\partial_{\Delta D} \Pi^n[\delta\gamma] \geq 0 \Rightarrow f^n(\mathbf{t}_{coh}, \Delta D; D^n) \Delta D = 0, \quad -f^n(\mathbf{t}_{coh}, \Delta D; D^n) \geq 0, \quad \Delta D \geq 0 \end{aligned} \tag{6}$$

where

$$\mathbf{t}_{coh} = \partial_{[\![\mathbf{u}]\!]} G^n = \mathbf{t}^- = -\mathbf{t}^+, \quad f^n(\mathbf{t}_{coh}, \Delta D; D^n) = -\partial_{\Delta D} G^n([\![\mathbf{u}]\!], \Delta D; D^n) \tag{7}$$

are the cohesive traction vector, with components expressed in the global reference system, and the damage activation function, respectively, whose precise expression will be specified in the next Section for the particular cohesive model employed.

## 3. Linear softening mixed-mode cohesive model

The isotropic, linear softening mixed-mode cohesive model proposed in [7,26] is considered. However, the approach to the simulation of crack propagation discussed in this work is general and other cohesive models could be used within the proposed framework.

Let $\mathbf{Q}$ be the orthogonal matrix transforming a vector with components in the global reference system into the same vector with components in the crack local reference. Let $w_s$, $w_n$ be the opening and sliding components, respectively, of $\mathbf{w} = \{w_s, w_n\}^T = \mathbf{Q}[\![\mathbf{u}]\!]$, i.e., of the displacement discontinuity vector $[\![\mathbf{u}]\!]$ expressed in the local reference of the cohesive crack, and let $\mathbf{t} = \{t_s, t_n\}^T = \mathbf{Q}\mathbf{t}_{coh}$ be the cohesive traction vector in the same reference system, $t_s, t_n$ being the corresponding tangential and normal traction components. An effective opening displacement $w$ is defined as [7,26]:

$$w(\mathbf{w}) = \sqrt{w_n^2 + \beta^2 w_s^2} \tag{8}$$

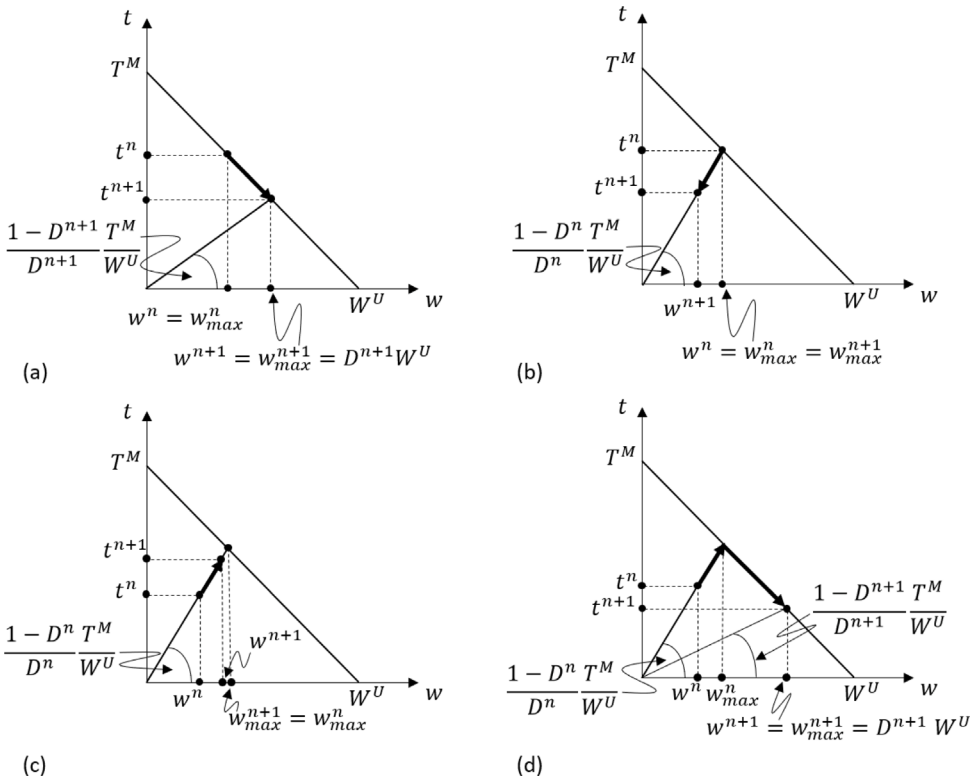


**Fig. 2.** Mixed-mode linear softening cohesive model. (a) Loading. (b) Unloading. (c) Elastic reloading. (d) Loading in the softening range.

$\beta$ being a material parameter allowing to assign different weights to the opening and sliding mechanisms in mixed-mode propagation, leading to different values of the limit cohesive tractions in pure mode I and pure mode II. The corresponding effective traction $t$ is defined in such a way that the following incremental work equivalence is satisfied:

$$t\dot{w} = t_s\dot{w}_s + t_n\dot{w}_n \tag{9}$$

leading to

$$t(\mathbf{t}) = \sqrt{t_n^2 + \frac{t_s^2}{\beta^2}}, \quad t_n = \frac{t}{w}w_n, \quad t_s = \beta^2\frac{t}{w}w_s \tag{10}$$

From (10), one can see that the value of $\beta = 1$ corresponds to the definition of a circular limit domain in the $t_n$–$t_s$ plane. Modifying the value of $\beta$ could be used to assign different peak strengths in the normal and shear directions. The effective traction–separation law with linear softening is illustrated in Fig. 2, where $D$ is the damage internal variable, $T^M$ and $W^U$ define the maximum effective traction and ultimate opening displacement, respectively, $k_{coh} < 0$ is the negative softening slope, $G_{cr} = 1/2(T^M W^U)$ is the cohesive fracture energy, and $w^n_{max}$ defines the maximum opening achieved up to time $t^n$, i.e. $w^n_{max} = \max_{0\le t\le t^n}\{w\}$, and $t^n_{max}$ the corresponding traction. Based on these definitions, the damage $D$ can be easily shown to satisfy the following relations:

$$w^n_{max} = D^n W^U, \quad t^n_{max} = (1-D^n)T^M, \quad t^n_{max} = \left(\frac{1-D^n}{D^n}\right)\frac{T^M}{W^U}w^n_{max} \tag{11}$$

Four cases are considered in Fig. 2:

(a) at time $t^n$ the pair $\{t^n, w^n\}$ defines a point on the softening branch and the point $\{t^{n+1}, w^{n+1}\}$ at the end of the step also defines a point on the softening branch (continuous loading during the time step). In this case $\Delta w > 0$ and the traction $t$ proceeds down along the softening branch with a positive damage increment and

$$D^{n+1} = \frac{w^n + \Delta w}{W^U}, \quad w^{n+1}_{max} = w^{n+1}, \quad t^{n+1} = (1-D^{n+1})T^M = \left(\frac{1-D^{n+1}}{D^{n+1}}\right)\frac{T^M}{W^U}w^{n+1} \tag{12}$$

(b) at time $t^n$ the pair $\{t^n, w^n\}$ defines a point on the softening branch and the final point $\{t^{n+1}, w^{n+1}\}$ defines a point on the unloading branch (unloading). In this case $\Delta w < 0$ and the traction $t$ proceeds down along the unloading branch with a zero damage increment and

$$D^{n+1} = D^n, \quad w^{n+1}_{max} = w^n_{max}, \quad t^{n+1} = \left(\frac{1-D^n}{D^n}\right)\frac{T^M}{W^U}w^{n+1} \tag{13}$$

(c) at time $t^n$ the pair $\{t^n, w^n\}$ defines a point on the unloading branch and the final point $\{t^{n+1}, w^{n+1}\}$ defines a point also on the unloading branch (elastic increment). In this case, one may have $\Delta w > 0$ or <0, but in both cases $0 \le w^n + \Delta w \le w^n_{max}$, and

$$D^{n+1} = D^n, \quad w^{n+1}_{max} = w^n_{max}, \quad t^{n+1} = \left(\frac{1-D^n}{D^n}\right)\frac{T^M}{W^U}w^{n+1} \tag{14}$$

(d) at time $t^n$ the pair $\{t^n, w^n\}$ defines a point on the unloading branch and the final point $\{t^{n+1}, w^{n+1}\}$ defines a point on the softening branch (reloading). In this case $\Delta w > 0$ with $w^n + \Delta w \ge w^n_{max}$ and the traction $t$ proceeds up along the unloading branch and then down along the softening branch, with $\Delta D > 0$ and

$$D^{n+1} = \frac{w^n + \Delta w}{W^U}, \quad w^{n+1}_{max} = w^{n+1}, \quad t^{n+1} = (1-D^{n+1})T^M = \left(\frac{1-D^{n+1}}{D^{n+1}}\right)\frac{T^M}{W^U}w^{n+1}_{max} \tag{15}$$

In the extreme case that $w^{n+1} < 0$, the crack closes and the two faces come in contact. This case is treated separately through a frictionless contact algorithm.

The cohesive potential $G^n(\mathbf{w}, \Delta D; D^n)$ is assumed to depend on $\mathbf{w}$ through the effective opening $w$ and, in the case of a linear softening model, takes the expression (note that the $n+1$ superscript is omitted, so that one has $D = D^n + \Delta D$)

$$G^n(w(\mathbf{w}), \Delta D; D^n) = \frac{1}{2}\left(\frac{1-D}{D}\right)\frac{T^M}{W^U}w^2(\mathbf{w}) + DG_{cr} \tag{16}$$

Based on this definition and on $(10)_{2,3}$, one has

$$\frac{\partial G^n}{\partial \mathbf{w}} = \frac{\partial G^n}{\partial w}\frac{\partial w}{\partial \mathbf{w}} = t\begin{Bmatrix} \beta^2\frac{w_s}{w} \\ \frac{w_n}{w}\end{Bmatrix} = \mathbf{t}, \quad \frac{\partial G^n}{\partial \Delta D} = -\frac{1}{2}\frac{1}{D^2}\frac{T^M}{W^U}w^2 + \frac{1}{2}T^M W^U \tag{17}$$

The expression of $\partial G^n/\partial \Delta D$ above, can be rewritten as

$$\frac{\partial G^n}{\partial \Delta D} = -\frac{1}{2}\frac{1}{(1-D)^2}\frac{W^U}{T^M}\left\{\left(\frac{1-D}{D}\frac{T^M}{W^U}w^2\right)^2 - \left[(1-D)T^M\right]^2\right\} \tag{18}$$

Making explicit the dependence on $\Delta D$ and the superscript $n+1$, and recalling the relations in $(11)_2$ and $(12)_3$, the partial derivative $\partial G^n/\partial \Delta D$ can be finally expressed in the form

$$\frac{\partial G^n}{\partial \Delta D} = -\frac{1}{2}\frac{1}{(1-D^n-\Delta D)^2}\frac{W^U}{T^M}\left[(t^{n+1})^2 - \left(t^{n+1}_{max}\right)^2\right] = f^n(\mathbf{t}, \Delta D; D^n) \tag{19}$$

Eq. (19) defines the damage activation function: a damage increment $\Delta D > 0$ can occur only if $f^n = 0$ in (19), where $t^{n+1}$ is computed according to $(12)_3$, under the loading assumption. The computation of the damage increment follows the usual return mapping scheme:

- for a prescribed opening $w^{n+1}$, compute $f^n_{trial}$ through (19) where $\Delta D = 0$ has been set and $t^{n+1}_{max} = t^n_{max}$;
- if $f^n_{trial} \le 0$ (or, alternatively, if $w^{n+1} \le w^n_{max}$), then $\Delta D = 0$ and $t^{n+1} = t^{n+1}_{trial}$;
- if $f^n_{trial} > 0$ (or, alternatively, if $w^{n+1} > w^n_{max}$), then $\Delta D > 0$ is computed by imposing that $w^{n+1} = (D^n + \Delta D)W^U$ and $t^{n+1}$ is obtained through Eq. $(12)_3$.

Recalling that $w_{max} = DW^U$, the consistent tangent stiffness matrix $\mathbf{D}_{coh} = \partial \Delta \mathbf{t}/\partial \Delta \mathbf{w}$ also takes different expressions depending on the loading/unloading nature of the step:

$$\mathbf{D}^{n+1}_{coh} = \begin{cases} -\left(\frac{1-D}{D}\right)k_{coh}\begin{bmatrix}\beta^2 & 0\\ 0 & 1\end{bmatrix} & \text{if } f^n(t, \Delta D; D^n) < 0 \\ -\left(\frac{1-D}{D}\right)k_{coh}\begin{bmatrix}\beta^2 & 0\\ 0 & 1\end{bmatrix} + \frac{k_{coh}}{D}\begin{bmatrix}\beta^4\frac{w_s^2}{w^2} & \beta^2\frac{w_s w_n}{w^2}\\ \beta^2\frac{w_s w_n}{w^2} & \frac{w_n^2}{w^2}\end{bmatrix} & \text{if } f^n(t, \Delta D; D^n) = 0 \end{cases} \tag{20}$$

## 4. Space discretization of the variational statement

### 4.1. Finite element formulation

The derivation of the discretized form of the conditions in (5) closely follows the approach presented in [32]. Only a brief account is given here, while further details can be found in [32].

The problem domain is discretized by $n_e$ polygonal elements $\Omega_e$ with a linear displacement model over the element edges. In the initial mesh, the initial crack $\Gamma$ is treated as an external boundary, so that the crack path runs along element edges. 2-node cohesive interface elements $\Gamma_e$ are then introduced along the crack path, with a linear modeling of the crack opening displacement.

Independent modeling of local displacements, strains and stresses is defined over each element $\Omega_e$ (note that the element subscript $e$ is omitted to simplify the notation wherever not strictly necessary):

$$\begin{aligned}\mathbf{u}\left(\boldsymbol{\xi}\right) &\approx \mathbf{u}^h\left(\boldsymbol{\xi}\right) &&= \mathbf{N}_u\left(\boldsymbol{\xi}\right)\hat{\mathbf{u}}\\ \boldsymbol{\varepsilon}\left(\boldsymbol{\xi}\right) &\approx \boldsymbol{\varepsilon}^h\left(\boldsymbol{\xi}\right) &&= \mathbf{N}_\varepsilon\left(\boldsymbol{\xi}\right)\hat{\boldsymbol{\varepsilon}}\\ \boldsymbol{\sigma}\left(\boldsymbol{\xi}\right) &\approx \boldsymbol{\sigma}^h\left(\boldsymbol{\xi}\right) &&= \mathbf{N}_\sigma\left(\boldsymbol{\xi}\right)\hat{\boldsymbol{\sigma}}\end{aligned} \tag{21}$$

where $\mathbf{u}^h$, $\boldsymbol{\varepsilon}^h$, and $\boldsymbol{\sigma}^h$ are approximations for displacements, strains, and stresses, respectively, $\boldsymbol{\xi}$ denotes a system of element intrinsic coordinates, and $\hat{\mathbf{u}}$, $\hat{\boldsymbol{\varepsilon}}$, and $\hat{\boldsymbol{\sigma}}$ are vectors of parameters. $\mathbf{N}_u$, $\mathbf{N}_\varepsilon$, and $\mathbf{N}_\sigma$ are matrices of shape functions defined in $\Omega_e$, whose dimensions in 2D are, respectively, $2\times n_u$, $3\times n_\varepsilon$ and $3\times n_\sigma$, $n_u$, $n_\varepsilon$ and $n_\sigma$ being the numbers of parameters describing the corresponding approximate field. Each of the shape functions in $\mathbf{N}_u$ is equal to one at an element node and equal to zero in all the other nodes and the resulting displacement field is continuous across adjacent elements. While the displacement parameters $\hat{\mathbf{u}}$ take the meaning of nodal displacements, $\hat{\boldsymbol{\varepsilon}}$ and $\hat{\boldsymbol{\sigma}}$ are just interpolation parameters with no special meaning and the resulting strain and stress fields are discontinuous across elements. The crack opening displacement $\mathbf{w}$ in the crack reference frame is also discretized over each interface element by linear shape functions in terms of the two nodal values $\hat{\mathbf{w}}$:

$$\mathbf{w}(\zeta) = \mathbf{N}_w(\zeta)\hat{\mathbf{w}} \tag{22}$$

$\zeta$ being a local coordinate running along the interface element length.

To have that the scalar product between the strain and stress parameters correctly represents the element energy, it must be $n_\varepsilon = n_\sigma$ and

$$\hat{\boldsymbol{\sigma}}^T\hat{\boldsymbol{\varepsilon}} = \int_{\Omega_e}\boldsymbol{\sigma}^T\left(\boldsymbol{\xi}\right)\boldsymbol{\varepsilon}\left(\boldsymbol{\xi}\right)d\Omega = \hat{\boldsymbol{\sigma}}^T\left(\int_{\Omega_e}\mathbf{N}_\sigma^T\left(\boldsymbol{\xi}\right)\mathbf{N}_\varepsilon\left(\boldsymbol{\xi}\right)d\Omega\right)\hat{\boldsymbol{\varepsilon}} \tag{23}$$

This condition is satisfied, e.g., if

$$\int_{\Omega_e}\mathbf{N}_\sigma^T\left(\boldsymbol{\xi}\right)\mathbf{N}_\varepsilon\left(\boldsymbol{\xi}\right)d\Omega = \mathbf{I} \tag{24}$$

where $\mathbf{I}$ is the identity matrix with dimensions $n_\varepsilon\times n_\varepsilon$ and

$$\mathbf{N}_\sigma\left(\boldsymbol{\xi}\right) = \mathbf{N}_\varepsilon\left(\boldsymbol{\xi}\right)\left(\int_{\Omega_e}\mathbf{N}_\varepsilon^T\left(\boldsymbol{\xi}\right)\mathbf{N}_\varepsilon\left(\boldsymbol{\xi}\right)d\Omega\right)^{-1} = \mathbf{N}_\varepsilon\left(\boldsymbol{\xi}\right)\mathbf{G}^{-1} \tag{25}$$

From (23) one also has

$$\hat{\boldsymbol{\sigma}}^T\hat{\boldsymbol{\varepsilon}} = \int_{\Omega_e}\boldsymbol{\sigma}^T\left(\boldsymbol{\xi}\right)\mathbf{N}_\varepsilon\left(\boldsymbol{\xi}\right)d\Omega\hat{\boldsymbol{\varepsilon}} \Rightarrow \hat{\boldsymbol{\sigma}} = \int_{\Omega_e}\mathbf{N}_\varepsilon^T\left(\boldsymbol{\xi}\right)\boldsymbol{\sigma}\left(\boldsymbol{\xi}\right)d\Omega \tag{26}$$

The equations governing the discretized problem are obtained by enforcing the stationarity of the discretized version of the functional $\Pi^n$ in (3) with respect to the three sets of discretization parameters $\hat{\mathbf{u}}$, $\hat{\boldsymbol{\varepsilon}}$ and $\hat{\boldsymbol{\sigma}}$. After assembling the element contributions, from the conditions in $(6)_{1-3}$, one obtains:

$$\begin{aligned}&\partial_{\hat{\mathbf{u}}}\Pi^h = 0 \implies \mathbf{C}^T\hat{\boldsymbol{\sigma}} = \mathbf{F}_{ext} + \mathbf{F}_{coh}(\llbracket\hat{\mathbf{u}}\rrbracket, D^n, \Delta D) && \text{equilibrium}\\ &\partial_{\hat{\boldsymbol{\varepsilon}}}\Pi^h = 0 \implies \hat{\boldsymbol{\sigma}} = \mathbf{E}\hat{\boldsymbol{\varepsilon}} && \text{linear elastic constitutive law}\\ &\partial_{\hat{\boldsymbol{\sigma}}}\Pi^h = 0 \implies \hat{\boldsymbol{\varepsilon}} = \mathbf{C}\hat{\mathbf{u}} && \text{compatibility}\end{aligned} \tag{27}$$

where the following elemental vectors and matrices (omitting subscript $e$) have been introduced:
(*i*) $n_\varepsilon\times n_\varepsilon$ elasticity matrix

$$\mathbf{E} = \int_{\Omega_e}\mathbf{N}_\varepsilon^T\mathbf{D}^{el}\mathbf{N}_\varepsilon d\Omega \tag{28}$$

(*ii*) $n_\varepsilon\times n_u$ compatibility matrix (taking into account the definition of $\mathbf{G}$ in (25))

$$\mathbf{C} = \int_{\Omega_e}\mathbf{N}_\sigma^T\left(\mathcal{S}\mathbf{N}_u\right)d\Omega = \mathbf{G}^{-1}\int_{\Omega_e}\mathbf{N}_\varepsilon^T\left(\mathcal{S}\mathbf{N}_u\right)d\Omega = \mathbf{G}^{-1}\mathbf{A} \tag{29}$$

(*iii*) equivalent nodal external forces vector

$$\mathbf{F}_{ext} = \int_{\Omega_e}\mathbf{N}_u^T\mathbf{b}d\Omega + \int_{(\partial\Omega_{\bar{\mathbf{t}}})_e}\mathbf{N}_u^T\bar{\mathbf{t}}d\partial\Omega \tag{30}$$

(*iv*) equivalent nodal cohesive forces vector

$$\mathbf{F}_{coh}(\llbracket\hat{\mathbf{u}}\rrbracket, D^n, \Delta D) = \int_{(\Gamma_{coh})_e}\mathbf{N}_u^T\mathbf{t}_{coh}(\llbracket\hat{\mathbf{u}}\rrbracket, D^n, \Delta D)d\Gamma \tag{31}$$

Finally, the stationarity with respect to $\Delta D$ leads to the damage loading–unloading conditions in $(6)_4$, to be enforced locally at the integration points of the cohesive interface elements.

By substituting $(27)_{2,3}$ in $(27)_1$ and assembling the contribution of all elements, one has

$$\mathbf{K}^c\hat{\mathbf{u}} - \mathbf{F}_{coh}([\![\hat{\mathbf{u}}]\!], D^n, \Delta D) = \mathbf{F}_{ext}, \quad \text{with } \mathbf{K}^c = \mathbf{C}^T\mathbf{E}\mathbf{C} \tag{32}$$

The system in (32), together with the damage loading–unloading conditions in $(6)_4$, defines the nonlinear finite-step equilibrium problem to be solved iteratively by a Newton–Raphson scheme, using the tangent stiffness matrix of the cohesive model defined in (20). $\mathbf{K}^c$ in (32) is the stiffness matrix of the linear elastic bulk material, consistent with the displacement and strain models. For the individual VE, this symmetric and positive semi-definite matrix has dimensions $n_u \times n_u$, $n_u$ being the number of nodal displacement Degrees Of Freedom (DOFs). When in an element $n_u - n_\varepsilon \leq 3$, $\mathbf{K}_e^c$ is 3 times singular, where the singular modes correspond to the three independent rigid-body motions. When $n_u - n_\varepsilon > 3$, $\mathbf{K}^c$ is more than 3 times singular, with the possible insurgence of zero-energy (hourglass) modes that need to be stabilized. Once the nodal displacements $\hat{\mathbf{u}}$ have been computed and taking into account Eq. (26), the approximate strain and stress fields can be derived, respectively, as

$$\begin{aligned}
&\boldsymbol{\varepsilon}^h(\boldsymbol{\xi}) = \mathbf{N}_\varepsilon(\boldsymbol{\xi})\hat{\boldsymbol{\varepsilon}} = \mathbf{N}_\varepsilon(\boldsymbol{\xi})\mathbf{C}\hat{\mathbf{u}} \\
&\boldsymbol{\sigma}^h(\boldsymbol{\xi}) = \mathbf{N}_\sigma(\boldsymbol{\xi})\hat{\boldsymbol{\sigma}} = \mathbf{N}_\sigma(\boldsymbol{\xi})\int_{\Omega_e}\mathbf{N}_\varepsilon^T(\boldsymbol{\xi})\boldsymbol{\sigma}(\boldsymbol{\xi})\,d\Omega = \mathbf{N}_\sigma(\boldsymbol{\xi})\int_{\Omega_e}\mathbf{N}_\varepsilon^T(\boldsymbol{\xi})\mathbf{D}^{el}\boldsymbol{\varepsilon}^h(\boldsymbol{\xi})\,d\Omega
\end{aligned} \tag{33}$$

### 4.2. Virtual element formulation

Let $\boldsymbol{\xi} = \{\xi, \eta\}^T$ define an element non-dimensional local Cartesian coordinate system with

$$\xi = \frac{x - x_G}{h_e}, \quad \eta = \frac{y - y_G}{h_e} \tag{34}$$

where $x_G$ and $y_G$ are the global coordinates of the element centroid, and $h_e$ is the maximum element diameter. It is important to note that here the coordinate transformation is linear whatever the element shape, in contrast to the standard isoparametric approach, where a nonlinear geometry mapping is required for non-regular shapes. This is a key ingredient for the almost complete insensitivity of VEs to distortion.

In the VEM, the displacement shape functions $\mathbf{N}_u$ are not explicitly known inside the element. The displacement model is assumed to contain polynomials of degree $k$ plus other unknown functions whose exact knowledge is not required. An element of this kind is therefore referred to as a Virtual Element (VE). In this work, we consider polygonal VEs of arbitrary shape and number of edges, with a linear interpolation of displacements on the edges. For this reason, this is a $k = 1$ VEM. While displacements are completely known on the boundary when their nodal values are known, displacements in the element interior remain unknown.

The key operator in the VEM is the compatibility matrix $\mathbf{C}$ defined in Eq. (29), in which the matrix $\mathbf{G}$ is directly computable once the strain shape functions $\mathbf{N}_\varepsilon$ are defined. In contrast, the computation of the matrix $\mathbf{A}$ is not obvious, since it contains the displacement shape functions $\mathbf{N}_u$, unknown in the element interior. To overcome the problem, one can integrate $\mathbf{A}$ by parts:

$$\mathbf{A} = \int_{\Omega_e}\mathbf{N}_\varepsilon^T(\boldsymbol{S}\mathbf{N}_u)\,d\Omega = \int_{\partial\Omega_e}(\mathbf{n}\mathbf{N}_\varepsilon)^T\mathbf{N}_u d\partial\Omega - \int_{\Omega_e}(\boldsymbol{S}^T\mathbf{N}_\varepsilon)^T\mathbf{N}_u d\Omega = \mathbf{A}_1 + \mathbf{A}_2 \tag{35}$$

The first term $\mathbf{A}_1$ in Eq. (35) is computable, as it results from the boundary integral of known quantities, as $\mathbf{N}_u$ is a linear polynomial on the boundary. In contrast, $\mathbf{A}_2$ contains an integral to be computed over the element interior, where the displacement model $\mathbf{N}_u$ is unknown. In the special cases that the strain model $\mathbf{N}_\varepsilon$ is constant or divergence-free, $\boldsymbol{S}^T\mathbf{N}_\varepsilon$ vanishes and one has $\mathbf{A} = \mathbf{A}_1$. In the case of non-divergence-free strain models and for the present $k = 1$ formulation, $\mathbf{A}_2$ can be computed by projecting the unknown displacement field onto a linear polynomial, according to the technique proposed in [31,37]. This technique has also been used in the present work for the computation of $\mathbf{A}_2$, following the implementation proposed in [32]. The domain integral for the computation of $\mathbf{A}_2$ is computed through a subtriagulation of the VE. The boundary integral in $\mathbf{A}_1$ is computed using a Gauss–Lobatto integration based on the nodes at the ends of each edge. Once the compatibility matrix $\mathbf{C}$ and the elastic matrix $\mathbf{E}$ have been computed, the local VEM consistent stiffness matrix $\mathbf{K}^c$ can be obtained by Eq. $(32)_2$.

### 4.3. Self-stabilized virtual element formulation

The element consistent stiffness matrix $\mathbf{K}^c$ in (32) of the linear elastic bulk material is symmetric and positive semi-definite with dimensions $n_u \times n_u$. When $n_u - n_\varepsilon > 3$, $\mathbf{K}^c$ is more than 3 times singular and spurious hourglass modes may arise even in the assembled mesh. In this case, an element stabilization is required. In the case of quadrilateral elements, $n_u = 8$ and at least $n_\varepsilon = 5$ is required to obtain a stable element. Following [32], a complete linear polynomial is used to model all strain components, leading to $n_\varepsilon = 9$, so that an initially self-stabilized (i.e., not requiring stabilization) element is obtained:

$$\mathbf{N}_\varepsilon(\boldsymbol{\xi}) = \begin{bmatrix} 1 & 0 & 0 & \xi & 0 & 0 & \eta & 0 & 0 \\ 0 & 1 & 0 & 0 & \xi & 0 & 0 & \eta & 0 \\ 0 & 0 & 1 & 0 & 0 & \xi & 0 & 0 & \eta \end{bmatrix} \tag{36}$$

A rigorous proof of self-stability for this type of quadrilateral VEs has been provided in [36]. In this work, an initial mesh made of these quadrilateral VEs is always adopted. However, upon crack propagation, new edges are added to the elements crossed by the crack, so that the crack path is described by a piece-wise linear trajectory, along which cohesive interface elements are introduced, as it will be shown in the next Section. In this case, the number $n_u = 8$ of nodal DOFs is increased, while the number $n_\varepsilon = 9$ of

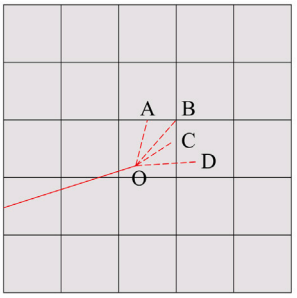


(a) Four possible propagation increments departing from a tip inside a quadrilateral element.

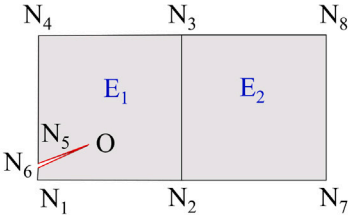


(b) Detail of two adjacent VEs.

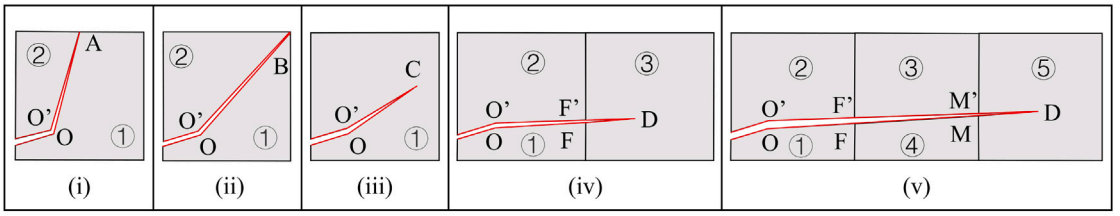


(c) Detail of four possible propagation increments.

**Fig. 3.** VE split strategy. (a) Possible propagation from a crack tip inside a VE. (b) Detail of VE containing the crack tip and of its adjacent VE. (c) Five possible crack propagation cases.

strain parameters remains the same. The consequence is that the balance between the $n_u$ displacements DOFs $\hat{\mathbf{u}}$ and the $n_\varepsilon$ strain parameters $\hat{\boldsymbol{\varepsilon}}$ is no longer satisfied when elements with 7 nodes (i.e., $n_u - n_\varepsilon = 14 - 9 = 5 > 3$) or more are considered. A stabilization will then become necessary for these elements also when a linear strain model is adopted. This will be discussed after the element split strategy will be illustrated in the next Section.

## 5. Virtual element split strategy

The VEM is ideally suited to deal with a propagating discontinuity through an existing mesh. The treatment of this usually critical event is made easy by the possibility offered by the VEM to smoothly add an arbitrary number of nodes and edges in a FE mesh, splitting the existing elements and generating in this way highly distorted and possibly non-convex elements, at the same time preserving the desired level of accuracy and order of convergence. To illustrate the developed strategy, reference is made to an initially regular mesh of quadrilateral elements, but the same strategy could be applied to VEs with an arbitrary number of edges. The main idea of the element split strategy is to split or cut the elements crossed by the crack path, by adding new nodes and edges along the predicted crack path. In this way, the newly generated VEs become polygons with arbitrary shapes, with some edges aligned along the piece-wise linear crack path.

The solid red line in Fig. 3(a) represents the existing crack at the end of the previous step, with node $O$ located in correspondence of the mathematical crack tip. The coordinates $(x_O^n, y_O^n)$ of the old crack tip node $O$ are therefore known. The element containing the tip node $O$ in Fig. 3(a) is a VE with 7 nodes, created by the cutting of the original 4-node element in the previous step. The dashed red lines in the same figure define four possible straight crack propagation increments $\Delta a$ in the current step. The actual increment direction is defined by the crack propagation criterion that will be discussed in the next Section, while the length of $\Delta a$ is prescribed as an input quantity, varying with the problem size and brittleness, more brittle structural responses requiring smaller increments $\Delta a$. The coordinates $(x_O^{n+1}, y_O^{n+1})$ of the new mathematical crack tip node are defined by

$$\begin{bmatrix} x_O^{n+1} \\ y_O^{n+1} \end{bmatrix} = \begin{bmatrix} x_O^{n} \\ y_O^{n} \end{bmatrix} + \begin{bmatrix} \Delta a \cos\theta \\ \Delta a \sin\theta \end{bmatrix} \tag{37}$$

where $\theta$ denotes the crack propagation direction defined in the global coordinate system.

Points $A$, $B$, $C$ and $D$ in Fig. 3(a) are possible locations of the new crack tip at the end of the current step. The non-convex element numbered $E_1$ in Fig. 3(b), containing the previous crack tip node $O$, has 7 nodes numbered in counter-clockwise order $[N_1, N_2, N_3, N_4, N_5, O, N_6]$, while the neighbor virtual element $E_2$ is quadrilateral, with the 4 nodes $[N_2, N_7, N_8, N_3]$. The five possible element splitting cases (see the details in Fig. 3(c), where element $E_1$ and $E_2$ are shown) are illustrated below making

reference to a mesh of quadrilateral elements. However, the same five cases define the splitting strategy also in the case of elements of an arbitrary number of edges.

(i) The new crack tip $A$ is located exactly on the element edge, defined by nodes $N_3$ and $N_4$ in element $E_1$, or very close to it, within a tolerance of 10% of the average edge length $\bar{l}_e$, to avoid overly short edges that could compromise accuracy. In this case, two nodes are added: node $O'$ comes from the duplication of the previous crack tip node $O$, while the new crack tip node $A$ is connected to the nodes $N_3$ and $N_4$ of the previous edge. Therefore, the original element $E_1$ is cut into two elements labeled as ① and ② in Fig. 3(c), where the new crack tip is assumed to be exactly on the previously existing edge. The resulting element ① has 6 nodes $[N_1, N_2, N_3, A, O, N_6]$ with a non-convex angle, and its element number remains $E_1$, while element ② has 4 nodes $[N_5, O', A, N_4]$, and its element number is appended to the last one in the original element list. The element above element $E_1$ (not shown in the figure) now shares edge $N_4A$ with element ② and edge $AN_3$ with element ①, and becomes a 5-node element. If the new crack tip node $A'$ is not precisely on the edge $N_3N_4$, but very close to it, and if its distance from the edge is less than the tolerance of 10% of the average edge length $\bar{l}_e$, the new edges connecting the crack tip $A'$ with the nodes $N_3$ and $N_4$ are not collinear and the element is slightly deformed.

(ii) The new crack tip $B$ coincides with an original node of the element. When the new crack tip $B$ coincides, e.g., with the original node $N_3$ of an element $E_1$, only one node $O'$ is added to duplicate the previous crack tip node $O$. In this case, the element $E_1$ is split into two elements marked as ① and ② in Fig. 3(c). Element ① has 5 nodes $[N_1, N_2, N_3, O, N_6]$ with a non-convex angle, while element ② has 4 nodes $[N_5, O', N_3, N_4]$. The neighbor elements do not undergo any transformation in this case. The case where the new crack tip coincides with nodes $N_1$, $N_2$ or $N_4$ is treated in the same way. If the new crack tip is not exactly coincident with an already existing node, but very close to it, to within a tolerance of 20% of the average edge length, the closest node is moved to the new crack tip by updating the coordinates of the original node, without modifying the crack path.

(iii) The new crack tip $C$ is located in the interior of $E_1$. In this case, only element $E_1$ needs to be modified, being transformed into a 9-node element, with nodes $[N_1, N_2, N_3, N_4, N_5, O', C, O, N_6]$, by the addition of the new crack tip at node $C$ and of node $O'$ as a consequence of the duplication of the previous crack tip $O$.

(iv) The new crack tip $D$ is located in the interior of $E_2$. In this case, both elements $E_1$ and $E_2$ are modified and four new nodes are inserted. Besides the new crack tip node $D$ and node $O'$, duplicating the original tip $O$, the intersection nodes $F$ and $F'$ between the crack and the element edge $N_2N_3$ are also inserted. Element $E_1$ is cut into two elements, as shown in Fig. 3(c). Element ① has 5 nodes $[N_1, N_2, F, O, N_6]$ with a non-convex angle, keeping its element number $E_1$. The non-convex element ② has also 5 nodes $[N_5, O', F', N_3, N_4]$, and its element number is appended to the final number of the original element list. Moreover, element $E_2$ is transformed from a quadrilateral element into a 7-node non-convex element, with nodes $[N_2, N_7, N_8, N_3, F', D, F]$.

(v) The new crack tip $D$ is located in the interior of the element with the crack edge propagating through more than two elements. Compared with case (iv), the difference is that the neighbor element $E_2$ is divided into two elements by inserting other two new nodes $M$ and $M'$. Element ⑤, containing the new crack tip, is transformed into a 7-node non-convex element. A possible case where the new crack tip stops at an edge of element ⑤, or at one of the original element nodes, can be considered as the combination of this case (v) and of case(i) or case(ii).

It should be remarked that the split strategy illustrated above refers to a single crack propagating in a 2D domain. In this case, the computational cost is minimal, all the operations being limited only to the few elements crossed by the new crack increment. The costs associated to the cohesive interface elements, are exactly the same of a FEM approach. The element computations required for a VE are in general slightly more expensive than for a FE. However, order one quadrilateral VEs are perfectly compatible with bilinear FEs, and far from the region of the expected propagation, VEs can be conveniently replaced by FEs.

The situation is different in the case that more than one crack is nucleated. Multiple cracks can be treated in the same way as long as they do not intersect, while crack branching and/or coalescence would require a dedicated procedure.

Extension of the proposed splitting strategy to the 3D case is in principle possible, by considering polyhedral VEs. Additional difficulties have however to be expected for the geometrical description of the propagating fracture plane in view of the increased number of cases to be considered, due to the higher dimensionality of the space.

## 6. Hourglass stabilization

As shown in the previous Section, with the considered element split strategy crack propagation in an initial mesh of regular quadrilateral elements produces a number of 7-node and 9-node VEs of arbitrary shape. Based on the discussion on self-stabilization at the end of Section 4.3, though the initial quadrilateral elements are stable, the newly generated 7-node and 9-node VEs are not so and need be stabilized. To this purpose, a possibility is to modify the strain model in the interested VEs, considering higher order polynomials and, hence, a higher number of strain parameters $\hat{\boldsymbol{\varepsilon}}$. The drawback of this approach is that it would lead to a heterogeneous strain modeling across elements, with a locally higher computing cost due to the higher order polynomial terms that need be integrated in matrix $\mathbf{A}$ in (35). This would also imply a heterogeneity, difficult to justify, among neighboring elements in the stress-smoothing process that will be discussed in the next Section 7 for the computation of the stress state at the fictitious crack tip. As an alternative to this approach, the stabilization proposed in [32] for constant strain models is here adapted to the linear strain model considered in the present work, by using a quadratic displacement field to define the rigid and pure deformation modes. The resulting mesh will be made of self-stabilized elements, with some initially self-stable elements that have to be stabilized after being crossed by the crack. As long as the same strain model is used in all elements, this is not a problem since hourglass stabilization does not compromise the element performance and the stabilized element is convergent with the same order of convergence of the self-stabilized one. It is usually preferred to avoid stabilization because of the need to choose artificial stabilization parameters.

However, the possibility of significant activation of an hourglass mode practically vanishes when the element is embedded in a mesh of stable elements, as it is the case considered here. Moreover, the fact that the virtual element is initially self-stable reduces the number of possible hourglass modes, further mitigating the problem.

The basic idea is to define first the hourglass modes $\hat{\mathbf{u}}^H$, i.e. the $n_H$ independent combinations of nodal displacements spanning the kernel of the consistent stiffness matrix $\mathbf{K}^c$, then to add some artificial stiffness to them. This implies deriving the $n_u \times n_u$, with $n_u > 12$, hourglass matrix $\mathbf{H}$ such that

$$\hat{\mathbf{u}}^H = \mathbf{H}\hat{\mathbf{u}} \tag{38}$$

To this purpose, the vector of nodal displacements $\hat{\mathbf{u}}$ is expressed in terms of *natural* parameters $\hat{\mathbf{p}}^{D+R}$ and $\hat{\mathbf{p}}^H$, where the superscript $D+R$ denotes pure Deformation + Rigid body modes and $H$ denotes Hourglass modes:

$$\hat{\mathbf{u}} = \hat{\mathbf{u}}^{D+R} + \hat{\mathbf{u}}^H = \mathbf{T}^{D+R}\hat{\mathbf{p}}^{D+R} + \mathbf{T}^H\hat{\mathbf{p}}^H \tag{39}$$

In (39), $\mathbf{T}^{D+R}$ is a matrix whose $n_u - n_H$ columns represent combinations of nodal displacements defining pure deformation and rigid body modes, while $\mathbf{T}^H$ is the matrix whose $n_H$ columns define hourglass modes, with $(\mathbf{T}^{D+R})^T\mathbf{T}^H = \mathbf{0}$. From (38), one also has that it must be $\mathbf{H}\hat{\mathbf{u}}^{D+R} = \mathbf{0}$. Multiplying $\hat{\mathbf{u}}$ in (39) from the left by $(\mathbf{T}^{D+R})^T$, one has

$$(\mathbf{T}^{D+R})^T\hat{\mathbf{u}} = (\mathbf{T}^{D+R})^T\mathbf{T}^{D+R}\hat{\mathbf{p}}^{D+R} \tag{40}$$

Solving for $\hat{\mathbf{p}}^{D+R}$, replacing in (39) and solving for $\hat{\mathbf{u}}^H$, one finally obtains:

$$\hat{\mathbf{u}}^H = \hat{\mathbf{u}} - \mathbf{T}^{D+R}\hat{\mathbf{p}}^{D+R} = \underbrace{\left\{\mathbf{I} - \mathbf{T}^{D+R}\left[(\mathbf{T}^{D+R})^T\mathbf{T}^{D+R}\right]^{-1}(\mathbf{T}^{D+R})^T\right\}}_{\mathbf{H}}\hat{\mathbf{u}} \tag{41}$$

The hourglass matrix $\mathbf{H}$ is therefore known once $\mathbf{T}^{D+R}$ is known.

In the standard $k = 1$ VEM, a $k-1$ (i.e., constant) strain model is adopted, so that a linear displacement field completely defines the strains through linear compatibility, while the other unknown functions contained in $\mathbf{N}_u$ are responsible for the hourglass modes (see [32] for the stabilization in this case). In the present case, the strain field in (36) is linear, with $n_\varepsilon = 9$. In an element with seven nodes, such as the element $E_1$ in Fig. 3(b) containing the mathematical crack tip $O$, one has $n_u - n_\varepsilon = 14 - 9 = 5 > 3$ and the element must be stabilized. Since the strains are linear, they are completely defined through compatibility by a quadratic displacement field of the type

$$\mathbf{u}^h_{D+R}(\boldsymbol{\xi}) = \mathbf{N}_2(\boldsymbol{\xi})\hat{\mathbf{p}}^{D+R}, \text{ with } \mathbf{N}_2(\boldsymbol{\xi}) = \begin{bmatrix} 1 & 0 & \xi & 0 & \eta & 0 & \xi^2 & 0 & \xi\eta & 0 & \eta^2 & 0 \\ 0 & 1 & 0 & \xi & 0 & \eta & 0 & \xi^2 & 0 & \xi\eta & 0 & \eta^2 \end{bmatrix} \tag{42}$$

The same displacement field can be imagined to be defined by a matrix of virtual shape functions $\mathbf{N}_u(\boldsymbol{\xi})$ multiplying the nodal displacements $\hat{\mathbf{u}}^{D+R}$, defining pure deformation and rigid body modes, so that one can write

$$\mathbf{u}^h_{D+R}(\boldsymbol{\xi}) = \mathbf{N}_2(\boldsymbol{\xi})\hat{\mathbf{p}}^{D+R} = \mathbf{N}_u(\boldsymbol{\xi})\hat{\mathbf{u}}^{D+R} = \mathbf{N}_u(\boldsymbol{\xi})\mathbf{T}^{D+R}\hat{\mathbf{p}}^{D+R} \;\Rightarrow\; \mathbf{N}_2(\boldsymbol{\xi}) = \mathbf{N}_u(\boldsymbol{\xi})\mathbf{T}^{D+R} \tag{43}$$

Since the shape functions in $\mathbf{N}_u$ in (43) by definition take value 1 in their reference node, i.e. $\mathbf{N}_u(\boldsymbol{\xi}_i) = 1$, $\boldsymbol{\xi}_i$ being the coordinates of the $i-$th node, and 0 in all the other nodes, the relation in (43) provides a straightforward way to compute $\mathbf{T}^{D+R}$ and, hence, $\mathbf{H}$ from (41), by evaluating (43) at the element nodes. For instance, at node 1 one has

$$\mathbf{N}_2(\boldsymbol{\xi}_1) = \begin{bmatrix} 1 & 0 & \xi_1 & 0 & \dots & \eta_1^2 & 0 \\ 0 & 1 & 0 & \xi_1 & \dots & 0 & \eta_1^2 \end{bmatrix} = \begin{bmatrix} 1 & 0 & 0 & 0 & \dots & 0 & 0 \\ 0 & 1 & 0 & 0 & \dots & 0 & 0 \end{bmatrix}\mathbf{T}^{D+R} \tag{44}$$

This expression provides the first two rows of $\mathbf{T}^{D+R}$. The other rows can be computed similarly by evaluating $\mathbf{N}_2$ at the other nodes. The resulting $\mathbf{T}^{D+R}$ matrix has 12 columns, each column defining one of the 9 pure deformation modes corresponding to the adopted linear deformation model, or one of the three rigid body modes.

Once $\mathbf{T}^{D+R}$ and $\mathbf{H}$ have been computed, the element consistent stiffness matrix $\mathbf{K}^c_e$ is stabilized by adding a stabilization stiffness matrix $\mathbf{K}^s_e$ defined as (see [38])

$$\mathbf{K}^s_e = \mathbf{H}^T_e\boldsymbol{\Lambda}_e\mathbf{H}_e \tag{45}$$

with (see [38])

$$\boldsymbol{\Lambda}_e = \text{diag}\,[\boldsymbol{\Lambda}]_{ii} = \text{diag}\left[\max\left\{\left[\mathbf{K}^c_e\right]_{ii}, \frac{1}{9}\text{tr}\left(\mathbf{D}^{el}\right)\right\}\right] \tag{46}$$

In the equilibrium Eqs. (32), the assembled $\mathbf{K}^s$ is then added to $\mathbf{K}^c$

$$(\mathbf{K}^c + \mathbf{K}^s)\hat{\mathbf{u}} - \mathbf{F}_{coh}(\llbracket\hat{\mathbf{u}}\rrbracket, D^n, \Delta D) = \mathbf{F}_{ext} \tag{47}$$

This procedure can be used for the stabilization of any 2D VE with $k = 1$, $\mathbf{N}_\varepsilon(\boldsymbol{\xi})$ defined by complete linear polynomials (i.e. with $n_\varepsilon = 9$), and with a number of nodes $\geq 7$.

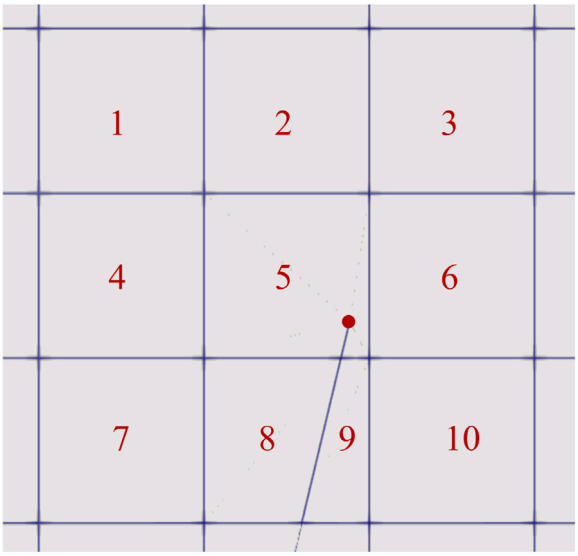


**Fig. 4.** VE patch containing the current mathematical crack tip.

## 7. Implementation of crack propagation algorithm

### 7.1. Crack propagation criterion

Following a common criterion, crack propagation is assumed to occur initially in mode I, i.e., when the maximum principal stress at the current mathematical crack tip exceeds the cohesive strength $T^M$. Accordingly, the propagation takes place in the direction orthogonal to the maximum principal stress direction. The following operations are then carried out within the considered time step.

- At time $t^n$, the current position $(x_O^n, y_O^n)$ of the mathematical crack tip $O$ is assumed to be known. A new load increment is assigned and a trial solution with the current crack configuration is computed, assuming that no propagation takes place in the time step and solving the nonlinear problem defined in (47).
- The maximum principal stress $\sigma^{max}$ at the mathematical tip of the existing cohesive crack is computed and compared to $T^M$.
  - If $\sigma^{max} > T^M$, then a crack increment $\Delta a$ is prescribed in the direction normal to the direction of $\sigma^{max}$.
  - If $\sigma^{max} \leq T^M$, then no propagation occurs in the considered time step, a new load increment is assigned and a new trial solution is computed.
- In the case that $\sigma^{max} > T^M$ at the current mathematical crack tip, the mesh is updated, integrating the new crack increment $\Delta a$ in the existing mesh, by using the VE split strategy described in Section 5.
- A new solution is computed iteratively solving the nonlinear problem (47) for the updated crack configuration.

### 7.2. Computation of max principal stress at crack tip position

As illustrated in the previous subsection, both the crack propagation criterion and the direction of propagation are based on the accurate determination of $\sigma^{max}$. The adopted linear modeling of the element strain field and, through (25), of the stress field, allows for a higher order accuracy in the stress computation within the element. It should be noted that while in the VE interior displacements are unknown, the stress and strain fields are known everywhere in the element, thanks to their independent modeling (33). The stress field resulting from $(33)_2$ is however discontinuous across elements. A smoother, more accurate stress field in the element containing the current mathematical crack tip, to be used in the crack propagation criterion, is obtained by the following procedure.

- Define the patch $\bar{\Omega}_e$ of the element containing the current mathematical crack tip and of its neighbor elements (Fig. 4).
- For all the elements $e$ in the patch $\bar{\Omega}_e$:
  - After the nodal displacements $\hat{\mathbf{u}}$ have been computed, compute the strain parameters $\hat{\boldsymbol{\varepsilon}} = \mathbf{C}\hat{\mathbf{u}}$ for all the elements in the patch $\bar{\Omega}_e$.
  - Compute the stress components at the element integration points $\boldsymbol{\xi}_g \in \bar{\Omega}_e$ : $\boldsymbol{\sigma}_e^h(\boldsymbol{\xi}_g) = \mathbf{D}^{el}\mathbf{N}_\varepsilon(\boldsymbol{\xi}_g)\hat{\boldsymbol{\varepsilon}}$.

**Table 1**
Wedge Splitting Test. Mechanical parameters of bulk and cohesive materials.

| Parameters | Symbol | Value |
|---|---|---|
| Young modulus of bulk material | $E$ | 25200 MPa |
| Poisson ratio | $\nu$ | 0.2 |
| Fracture energy | $G_c$ | 0.1 N/mm |
| Maximum traction stress | $T^M$ | 3.3 MPa |
| Maximum opening of the cohesive interface | $W^U$ | 0.061 mm |

  - Using (26), compute the stress parameters $\hat{\boldsymbol{\sigma}}_e = \sum_{g=1}^{n_g} \Omega_e \mathbf{N}_\varepsilon^T(\boldsymbol{\xi}_g)\, \boldsymbol{\sigma}_e^h(\boldsymbol{\xi}_g)\, w_g$, where $n_g$ is the number of element integration points of the considered element $e$ and $w_g$ are the integration weights at the same point.
  - Compute the stress $\boldsymbol{\sigma}_e^h(\boldsymbol{\xi}_a)$ at the nodes of the element containing the crack tip: $\boldsymbol{\sigma}_e^h(\boldsymbol{\xi}_a) = \mathbf{N}_{\sigma_e^h}(\boldsymbol{\xi}_a)\hat{\boldsymbol{\sigma}}_e$, where $\boldsymbol{\xi}_a$ denotes nodal coordinates.

- At each node of the element containing the crack tip, compute the average $\bar{\boldsymbol{\sigma}}(\boldsymbol{\xi}_a)$ of the nodal stresses of all elements in the patch sharing that node.
- For the element containing the crack tip, compute the modified stress parameters $\hat{\hat{\sigma}}$ by a linear projection, based on the averaged nodal values $\bar{\boldsymbol{\sigma}}(\boldsymbol{\xi}_a)$, minimizing the difference

$$\min_{\hat{\hat{\sigma}}} = \sum_{a=1}^{n_{nodes}} \left[\bar{\mathbf{N}}_\sigma(\boldsymbol{\xi}_a)\hat{\hat{\sigma}} - \bar{\boldsymbol{\sigma}}(\boldsymbol{\xi}_a)\right]^T \left[\bar{\mathbf{N}}_\sigma(\boldsymbol{\xi}_a)\hat{\hat{\sigma}} - \bar{\boldsymbol{\sigma}}(\boldsymbol{\xi}_a)\right] \tag{48}$$

  where $n_{nodes}$ is the number of the element nodes and $\bar{\mathbf{N}}_\sigma(\boldsymbol{\xi}) = \mathbf{N}_\varepsilon(\boldsymbol{\xi})$ has been set, with $\mathbf{N}_\varepsilon(\boldsymbol{\xi})$ defined in (36).
- Compute the smoothed stress $\bar{\boldsymbol{\sigma}}(\boldsymbol{\xi}_O)$ at the mathematical crack tip, to be used in the crack propagation criterion: $\bar{\boldsymbol{\sigma}}(\boldsymbol{\xi}_O) = \bar{\mathbf{N}}_\sigma(\boldsymbol{\xi}_O)\hat{\hat{\sigma}}$.

## 8. Numerical tests

Based on the proposed self-stabilized VEM incorporating a crack propagation model, five numerical tests taken from the literature are carried out to investigate the method performance and accuracy. In the first two tests, the results of the VEM numerical simulations are compared with the results obtained with two popular numerical techniques, namely an X-FEM approach for a mode-I splitting test (see Section 8.1), and a phase-field approach to fracture for the simulation of a mode-II shear test (see Section 8.2). In the remaining three tests, the results of the VEM numerical simulations are compared with the experimental results of three mixed-mode crack propagation tests involving an L-shaped panel test (Section 8.3) and two three-point bending tests with an off-centered notch placed in two different positions (Section 8.4).

### 8.1. Wedge splitting test

A mode-I wedge splitting test with the geometry and boundary conditions shown in Fig. 5 (units are in mm) is considered first. The wedge splitting experiment in [39] was intended to test the fracture toughness of concrete materials. The specimen has an initial crack length of 115 mm. Opening vertical displacements are applied symmetrically at the two wedge edges, and the center point of the right edge is fixed both horizontally and vertically. The crack mouth opening displacement (CMOD) is measured at the mouth of the initial notch. The specimen has been initially discretized by 6622 elements of typical size $h_e = 2.5$ mm. The element in front of the initial crack tip is a 5-node rectangular element, while the other elements are regular 4-node quadrilateral elements ( Fig. 6). The hanging node at the middle of the left edge of the 5-node element (in red in Fig. 6) is the initial crack tip node. The mode-I crack propagation path is rectilinear due to the symmetry of boundary conditions and applied displacement load. During crack growth, the crack will propagate through the elements interior, dividing them into two parts and generating new elements.

In order to compare with the results of an X-FEM approach, the material parameters used in [26] have been adopted for the simulations. The bulk material is linear elastic, with Young's modulus $E = 25200$ MPa and Poisson ratio $\nu = 0.2$. The parameters of the cohesive model are: fracture energy $G_c = 0.1$ N/mm, maximum traction $T^M = 3.3$ MPa and maximum opening of the cohesive interface $W^U = 0.061$ mm (see Table 1). Since the specimen has a thickness of 97 mm, plane strain conditions are assumed. A mixed-mode coupling coefficient $\beta = 1$ is assumed. A total displacement of 0.23 mm per wedge side (0.46 mm of crack mouth opening), with a prescribed increment $\Delta\bar{\mathbf{u}} = 0.005$ mm per side at each time step, is imposed. A crack increment $\Delta a = 3/4\bar{l}_e$, where $\bar{l}_e$ is the average length of the element edge, is imposed at each time step if the crack propagation criterion is satisfied.

During propagation, the crack goes through the original mesh, cutting the elements located along the crack path. As depicted in Fig. 7(a), node A represents the old crack tip, node B is the new crack tip after propagation, and the dashed red line AB is the increment $\Delta a$ of the crack path. During this process, the old crack tip node A is duplicated (A' is the new node), and two new intersection nodes C and C' are created between the crack edge and the edge of the old element, as shown in Fig. 7(b). The crack increment AB separates the old element into two 5-node elements and the new element containing the new crack tip becomes a 7-node non-convex element, where node B coincides with the new crack tip position. For this wedge splitting test, the obtained crack path is almost perfectly straight. The computed reaction force and prescribed CMOD are plotted in Fig. 8. The VEM numerical results are in good agreement with the numerical results in [26], obtained by an X-FEM modeling of the displacement discontinuity with the same material parameters.

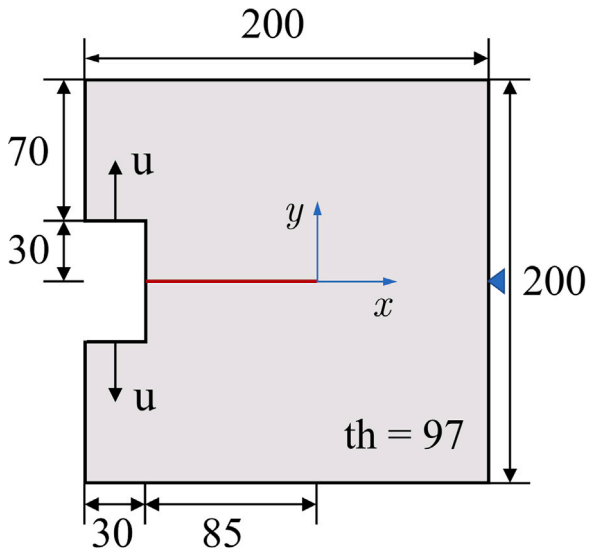


**Fig. 5.** Wedge Splitting Test. Geometry (mm) and boundary conditions. $th$ denotes specimen thickness.

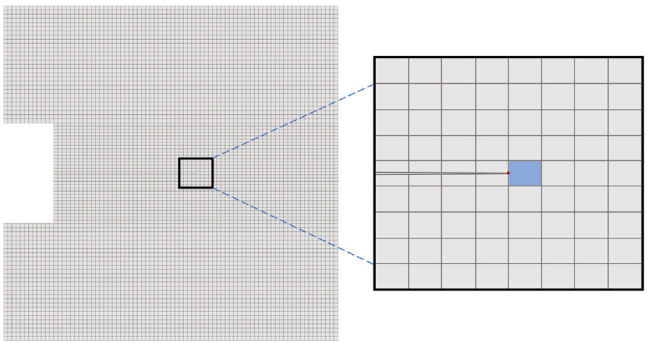

**Fig. 6.** Wedge Splitting Test. Finite element mesh and detail of crack tip region.

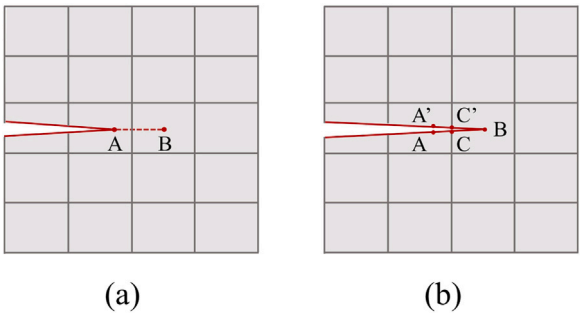


**Fig. 7.** Wedge splitting test. Element split procedure and crack propagation through the elements.

### *8.2. Single edge notched specimen under shear*

The single edge notched (SEN) specimen under shear test is analyzed for comparison with a phase-field numerical approach to the simulation of mode-II crack propagation. The geometry of the specimen is shown in Fig. 9. The dimension of the single edge notched specimen is $2 \times 2 \times 1$ mm with a 1 mm original notch. The bottom edge of the specimen is completely constrained in both horizontal and vertical directions. A rightward horizontal displacement is applied at the top edge, while its vertical displacement is constrained to be zero. The specimen is discretized by 8670 elements, with a typical element length $h_e = 0.0125$ mm of the refined

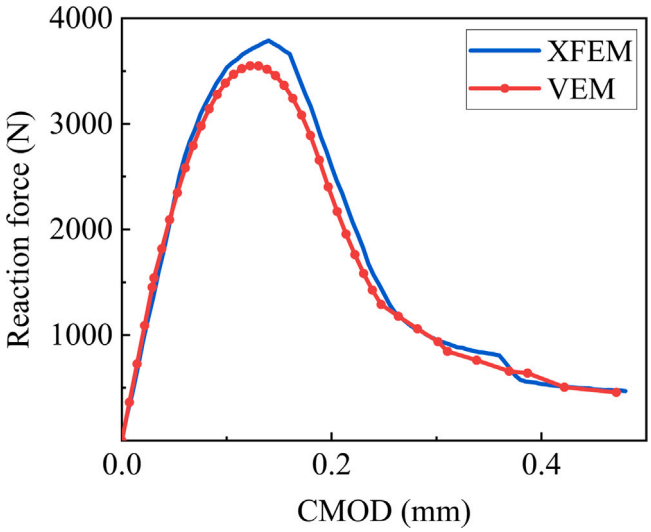


**Fig. 8.** Wedge splitting test. Reaction force vs. CMOD. Comparison of VEM results with XFEM [26] numerical results.

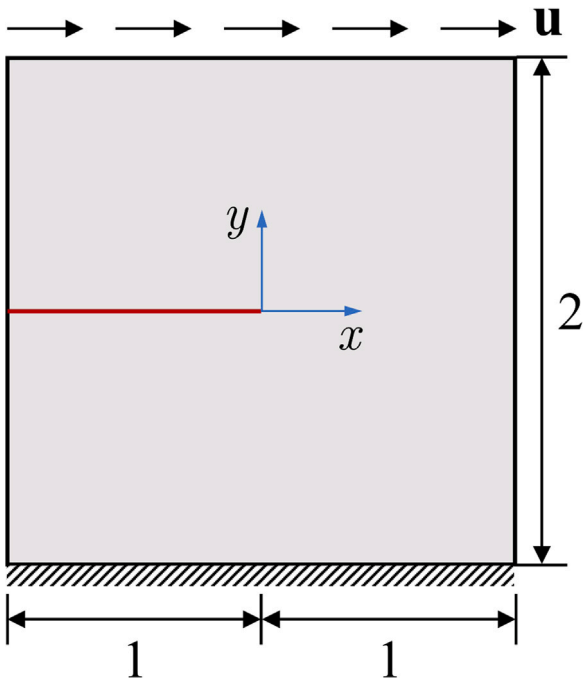


**Fig. 9.** SEN specimen under shear. Geometry (mm) and boundary conditions.

mesh, 1/2 of the length $h_e = 0.025$ mm in the region with the coarse mesh. The mechanical parameters for the bulk material and the cohesive model are displayed in Table 2. $\beta = 0.7$ is assumed for the coupling coefficient of the cohesive model. A constant crack increment $\Delta a = 0.025$ mm is prescribed with a horizontal displacement increment $\Delta \bar{\mathbf{u}} = 0.0003$ mm. Plane strain conditions are assumed.

The crack path predicted by the proposed linear-strain self-stabilized VEM model is displayed as the red curve in Fig. 10, while the black curve corresponds to the crack path produced by the Phase-Field Model (PFM) in [40]. The results obtained by the two methods are in good agreement. The details of the element split and crack path in a zoomed region of the VEM model are shown in Fig. 11.

The predicted reaction force-top displacement curve is plotted in Fig. 11, where it is compared with the numerical results based on the PFM (see [40]). The PFM crack path is a graphical approximation of the results in [40], since the PFM produces a damage localization band and not a discrete discontinuity. At the beginning, the mechanical response is linear elastic. Before the response

**Table 2**
SEN specimen under shear. Mechanical parameters of bulk material and cohesive model.

| Parameters | Symbol | Value |
|---|---|---|
| Young modulus of bulk material | $E$ | 210000 MPa |
| Poisson ratio | $\nu$ | 0.3 |
| Fracture energy | $G_c$ | 2.7 N/mm |
| Maximum traction stress | $T^M$ | 650 MPa |
| Maximum opening of the cohesive interface | $W^U$ | 0.0046 mm |

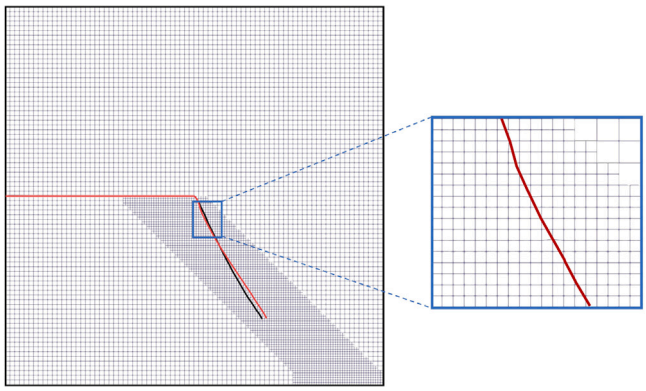

**Fig. 10.** SEN specimen under shear. Comparison of crack path obtained by the VEM (red curve) and by the PFM (black curve approximating the damage localization band). The zoomed-in box shows details of element splitting due to crack propagation.

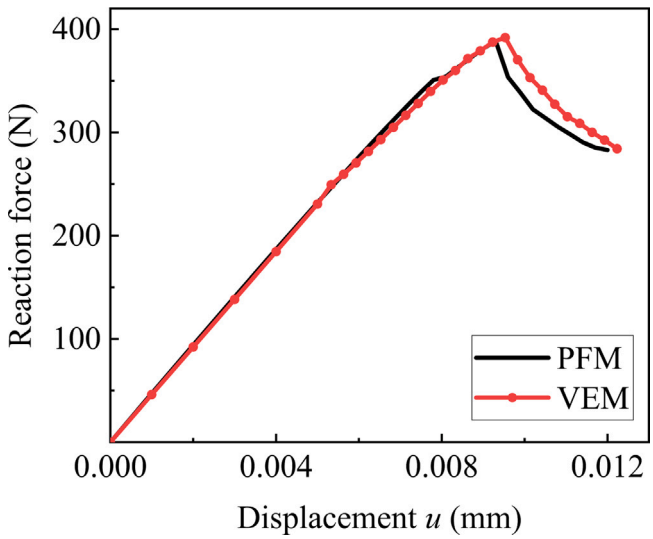


**Fig. 11.** SEN specimen under shear. Reaction force vs. imposed displacement obtained by the VEM (red curve) and by the PFM (black curve) in [40]. (For interpretation of the references to color in this figure legend, the reader is referred to the web version of this article.)

peak is achieved, there is a slight drop of the elastic modulus. During this stage, the process zone continuously expands. After the peak, the reaction force decreases due to crack propagation. The computed reaction-displacement curve is in good agreement with the one in [40].

### *8.3. L-shaped panel test*

A classical test with mixed-mode crack propagation in an L-shaped concrete panel [41] is simulated. The geometry and boundary conditions are shown in Fig. 12, with $L = 500$ mm, $L_1 = 220$ mm and a thickness of 100 mm. The bottom edge of the concrete panel is constrained both horizontally and vertically. An upward vertical displacement is applied at a point distant 30 mm from the right edge of the panel, while the displacement in the horizontal direction is free at the same point. Initially, the panel is discretized by

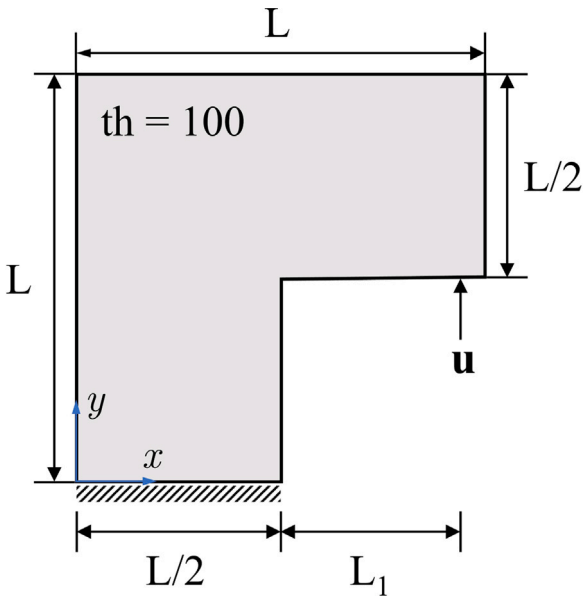


**Fig. 12.** L-shaped panel test. Geometry and boundary conditions.

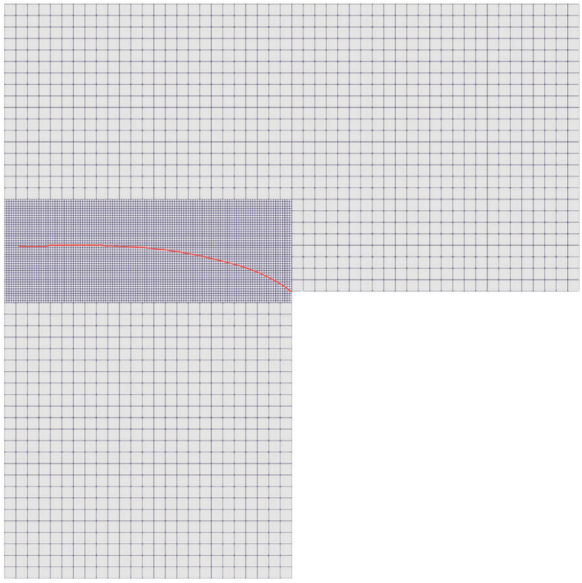

**Fig. 13.** L-shaped panel test. Mesh and computed crack path.

7275 elements of two different sizes, as shown in Fig. 13, where the red curve represents the numerical crack path obtained with the proposed VEM. The region where the crack is expected to propagate is meshed by fine elements, initially of 4 nodes each, of 2 mm edge length, while the area far from the center of the panel is meshed by coarse 4-node elements of 10 mm edge length, to improve the computational efficiency. It is worth noting that the mesh transition from coarse to fine elements is modeled straightforwardly by the VEM, by defining quadrilateral transition 8-node VEs, with 2 nodes per each of three edges and 6 nodes on the edge on the transition line. The edge with six nodes is shared by five fine 4-node elements. As soon as the crack starts to propagate, the mesh is updated according to the element split strategy described in Section 5 to accommodate the evolving displacement discontinuity within the existing mesh.

The used material parameters for the linear elastic bulk material and for the linear softening cohesive law, listed in Table 3, have been calibrated on the experimental curves in [41] (see also [42]). A coupling coefficient $\beta = 1$ has been adopted for the cohesive model. Plane stress conditions have been assumed. A crack increment $\Delta a = 3/2\bar{l}_e$, with $\bar{l}_e = 2$ mm, is imposed at each time step when the crack propagation criterion is satisfied, and $\Delta\bar{\mathbf{u}} = 0,0075$ mm.

**Table 3**
Mechanical parameters of bulk material and cohesive model in the L-shaped panel test.

| Parameters | Symbol | Value |
|---|---|---|
| Young modulus of bulk material | $E$ | 18000 MPa |
| Poisson ratio | $\nu$ | 0.18 |
| Fracture energy | $G_c$ | 0.075 N/mm |
| Maximum traction stress | $T^M$ | 2.6 MPa |
| Maximum opening of the cohesive interface | $W^U$ | 0.058 mm |

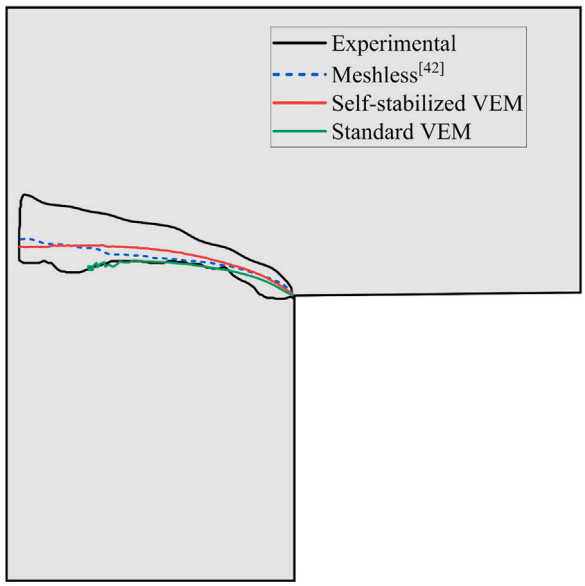


**Fig. 14.** L-shaped panel test. Comparison of numerical crack propagation paths with experimental results [41]: red curve = present VEM with initially self-stabilized elements (linear strains); green curve = standard stabilized VEM (constant strain); blue curve = Meshless Method [42]. (For interpretation of the references to color in this figure legend, the reader is referred to the web version of this article.)

The crack path based on the linear strain model (36) is shown in Fig. 13 (red curve). The obtained crack propagation trajectory is contained within the envelope of experimental crack propagation trajectories [41] and is compared with the numerical results (dashed blue curve) computed by a combined meshless-FEM approach in [42], as shown in Fig. 14. In addition, results obtained with the standard stabilized VEM with constant (instead of linear) strains, hourglass control, and the same nodal smoothing strategy are shown in the same figure (green curve). It can be observed that the proposed VEM based on the linear strain model (red curve) predicts a more accurate crack path than the one of the standard VEM with a constant strain model (green curve). For this latter case, the green curve shows that in an initial stage the crack grows smoothly, while in a later stage the path exhibits strong oscillations, with a premature stop due to lack of convergence. This is consistent with what has been observed for a similar type of standard VEM in [25].

The reaction force–displacement curve is shown in Fig. 15. The curve based on the linear strain VEM models is compared to the experimental ones [41], to the numerical results in [42] obtained by a meshless approach, and to the results obtained with a standard constant strain VEM with hourglass control. The reaction force response is linear elastic in the initial stage, with a rather steep softening branch after the peak. The red curve predicted by the VEM with linear strains fits fairly well the experimental results, while the green curve, relative to the standard VEM with a constant strain model and hourglass stabilization, overestimates the peak response and soon stops in the decreasing stage because of lack of convergence.

To investigate the robustness of the approach with respect to variations of the mesh size and of the crack increment size $\Delta a$, two parametric studies have been conducted. In the first case, the refined region of the L-shaped panel has been meshed with elements of different lengths of 4 mm, 3.33 mm, 2.5 mm, 2 mm, and 1.67 mm, with a total number of 2499, 3675, 5250, 7275 and 9750 elements, respectively, and with the same crack increment $\Delta a = 4$ mm. The results in terms of reaction force vs. displacement are plotted in Fig. 16. In the second parametric test, the same mesh with elements of average edge length $\bar{l}_e = 2$ mm in the refined region has been tested with crack increment lengths $\Delta a$ of $2\bar{l}_e$, $3/2\bar{l}_e$, $\bar{l}_e$, and $3/4\bar{l}_e$. The results in terms of reaction force vs. displacement are plotted in Fig. 17. It can be observed that the obtained responses are almost completely insensitive to the considered variations of mesh size and crack propagation increments, confirming the method robustness.

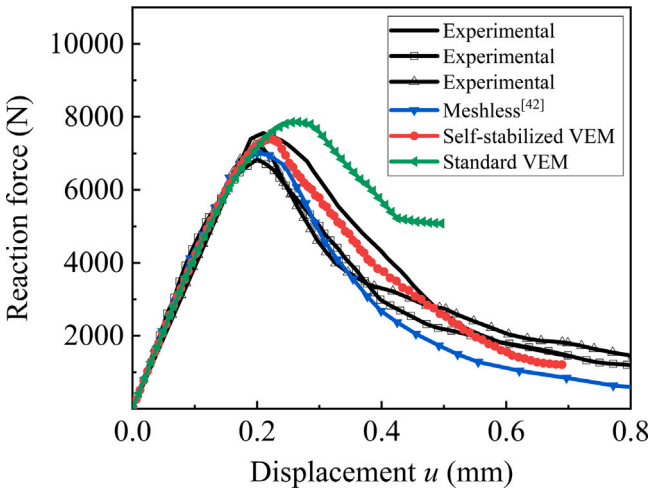


**Fig. 15.** L-shaped panel test. Reaction force vs. displacement. Comparison of VEM numerical results with experimental results [41]: red curve = present VEM with initially self-stabilized elements (linear strains); green curve = standard stabilized VEM (constant strains); blue curve = Meshless Method [42]; black curves = experimental. (For interpretation of the references to color in this figure legend, the reader is referred to the web version of this article.)

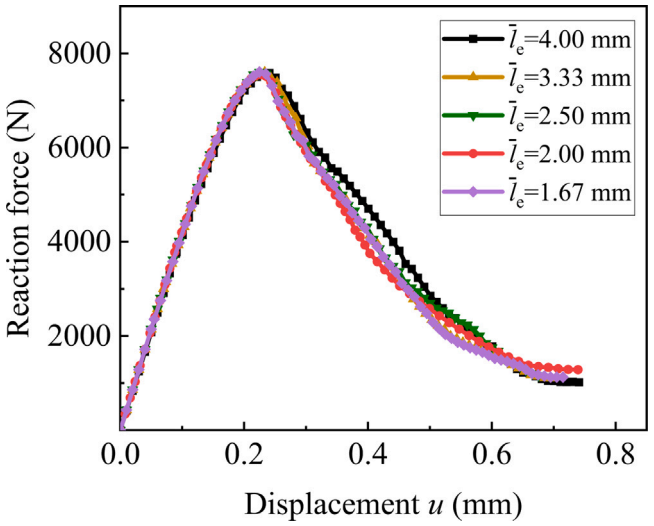


**Fig. 16.** L-shaped panel test. Reaction force vs. displacement responses for varying element lengths and constant crack propagation increment $\Delta a = 4$ mm.

### *8.4. Three-point-bending tests with off-centered initial notch*

Two three-point-bending tests of a simply supported specimen with off-centered initial notches experimentally tested in [43] are considered as the second type of mixed-mode crack propagation problem. The geometry and boundary conditions of the notched specimen are shown in Fig. 18. The length of the specimen is $S = 304.8$ mm, the width $W = 76.2$ mm and the thickness 28.6 mm. The length of the initial notch is 25.4 mm. The distance between the initial notch and the specimen midspan is $\alpha S$, where $\alpha$ is the off-center ratio. To investigate the effect of the initial notch location, two different off-center ratios of 1/6 and 1/4 are considered. The two ends at the bottom of the notch specimen are supported and fixed vertically, while they are free horizontally. At the top midspan, a vertical displacement is applied and at the same time its displacement is fixed in the $x$ direction. Initially, the notched specimen with the off-centered ratio 1/6 is meshed with 13528 4-node elements and the one with the off-centered ratio 1/4 with 14440 4-node elements, of tipical size $h_e = 2$ mm.

The mechanical parameters of the linear elastic bulk material and of the linear softening cohesive model are listed in Table 4. The coupling coefficient of the cohesive model is $\beta = 1$. The prescribed crack propagation and displacement increments are $\Delta a = 2$ mm and $\Delta \bar{\mathbf{u}} = 0.005$ mm, respectively. Plane strain conditions are assumed.

The crack paths predicted in the two considered cases based on the proposed VEM model are shown by the red curves in Fig. 19 and are in good agreement with the experimental results in [43] (black curves). To prevent possible instabilities due to snap-back

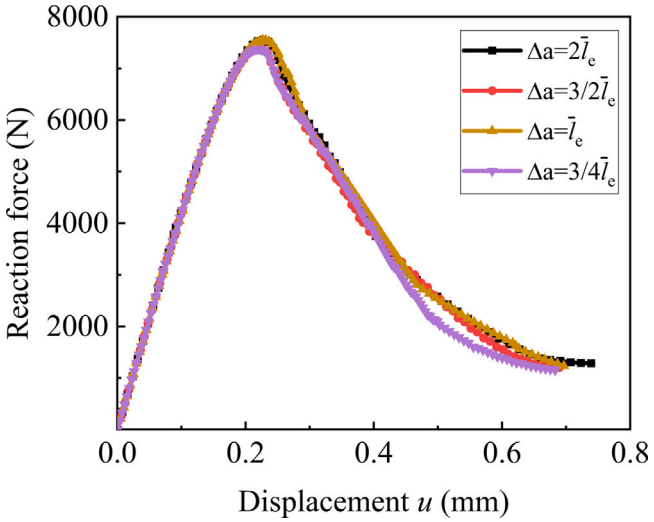


**Fig. 17.** L-shaped panel test. Reaction force vs. displacement curves for different crack increment length $\Delta a$ and constant mesh size.

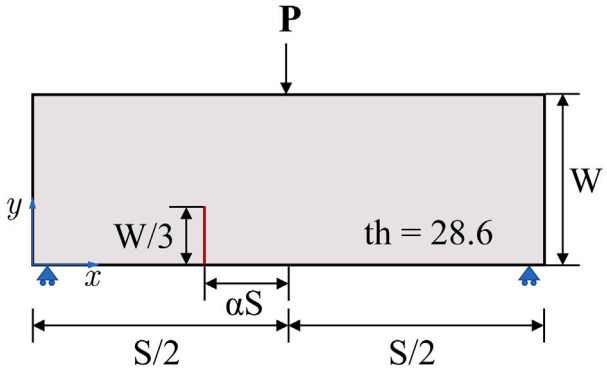


**Fig. 18.** Three-point-bending test with off-center notch. Specimen geometry and boundary conditions.

**Table 4**
Three-point-bending test with off-center notch. Mechanical parameters of bulk material and cohesive model.

| Parameters | Symbol | Value |
|---|---|---|
| Young modulus of bulk material | $E$ | 32800 MPa |
| Poisson ratio | $\nu$ | 0.18 |
| Fracture energy | $G_c$ | 0.08 N/mm |
| Maximum traction stress | $T^M$ | 2.8 MPa |
| Maximum opening of the cohesive interface | $W^U$ | 0.057 mm |

responses, the experimental tests have been conducted in a closed-loop testing machine with control of the Crack Mouth Opening Displacement (CMOD). The computed reaction force vs. CMOD curves for the two bending tests are plotted in Fig. 20. Also in this case, very good agreement with the experimental results in [43] has been achieved up to the peak response, while the initial softening branch is less accurate. This is probably due to the linear softening model used. The experimental initial softening branch is very steep, even in a Force-CMOD representation, becoming less steep in the final stage of failure. This type of response is difficult to reproduce with a cohesive model with a constant softening slope, as the one used here.

## 9. Conclusions

A numerical method for the simulation of mixed-mode cohesive crack propagation in 2D isotropic solids, based on the Virtual Element Method (VEM), has been proposed. The main novel contributions of the present work can be summarized as follows.

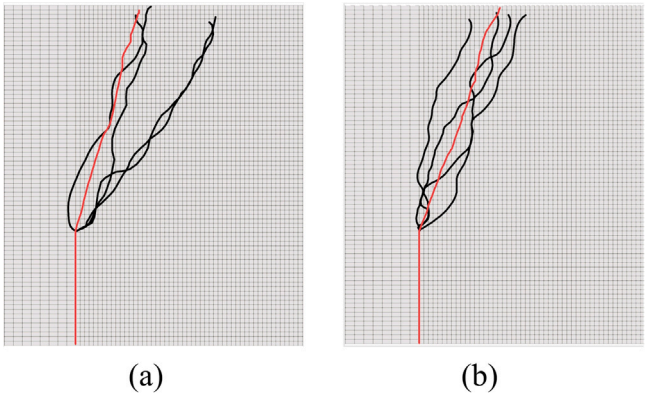


**Fig. 19.** Three-point-bending test with off-center notch. Crack paths for different off-centered ratios: (a) $\alpha = 1/6$ and (b) $\alpha = 1/4$. Red curve = VEM results; black curves = experimental results. (For interpretation of the references to color in this figure legend, the reader is referred to the web version of this article.)

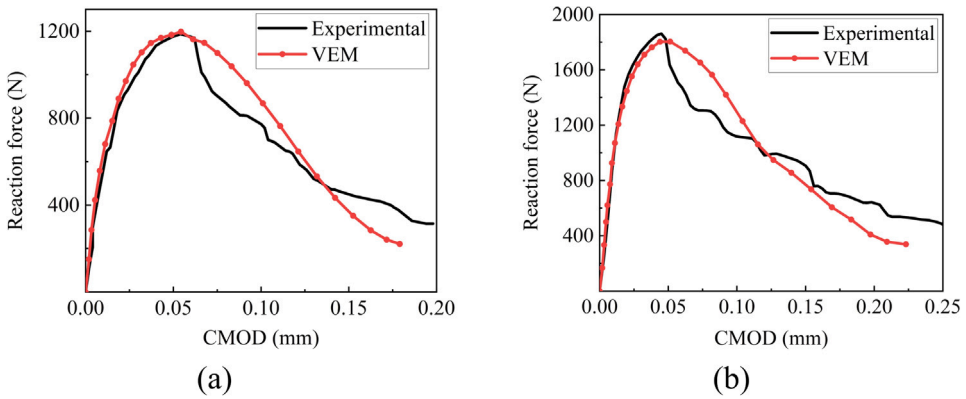


**Fig. 20.** Three-point-bending test with off-center notch. Reaction force vs. CMOD for different off-centered ratios: (a) $\alpha = 1/6$; (b) $\alpha = 1/4$. Red curve = VEM results; black curves = experimental results. (For interpretation of the references to color in this figure legend, the reader is referred to the web version of this article.)

- The proposed formulation is based on a consistent incremental finite-step version of Hu–Washizu variational principle incorporating the energy contribution of a linear softening mixed-mode cohesive crack model. The mixed variational formulation allows for an independent linear modeling of the strains. The stationarity conditions of the discretized functional are shown to return the problem governing equations, including the loading–unloading conditions for the cohesive model.
- A computationally inexpensive VE split strategy has been devised to accommodate the propagating cohesive crack increment into the VE mesh. Starting from a mesh of quadrilateral first-order VEs, new VEs with up to 9 nodes are generated. Linear cohesive interface elements are introduced between the newly created VE edges.
- Self-stabilized first-order VEs are used in the initial mesh. Self-stabilization is obtained by projecting the displacement gradients onto the assumed linear strain model. Upon crack propagation, the number of edges is increased in some VEs making them unstable. The new hourglass modes are stabilized by projecting displacements onto quadrilateral polynomials. Since the VEs were originally stable, the number of hourglass modes to be stabilized is smaller than in the standard VEM case.
- The adopted mixed-mode cohesive crack propagation criterion requires the stress evaluation at the mathematical cohesive crack tip. Better accuracy is achieved by exploiting the adopted linear strain modeling coupled to a stress smoothing procedure. The numerical tests have shown that more accurate predictions of the crack path in mixed-mode propagation can be obtained in this way.
- A number of reference numerical tests in mode-I, mode-II and mixed-mode, taken from the literature, has confirmed the accuracy and computational effectiveness of the proposed method. In particular, the beneficial role of the linear strain modeling in initially self-stabilized VEs has been assessed in comparison with the standard VEM.

In all the considered cases, accurate results have been obtained with a method simple to implement and computationally inexpensive. The propagating discontinuity is smoothly incorporated in the mesh by addition of nodes and edges to the interested elements, without touching the other elements and without caring about the distortion of the resulting new elements. This is possible because the VEs are almost completely insensitive to distortion (possible non-convex elements do not create problems) and can therefore take

any necessary shape without accuracy degradation. The possibility to define VEs with arbitrary number of nodes and edges can be conveniently exploited also to create the transition from a coarse to a finer mesh in the region where the propagation is expected, as shown in Section 8.3. Furthermore, unlike other methods, such as, e.g., Discontinuous-Galerkin approaches (see,e.g., [8–10]), in the VEM approach to fracture, a crack can propagate in any direction, not necessarily along element interfaces, and nodes are duplicated only in the elements crossed by the propagating crack, with only a minimal increase of the number of degrees of freedom.

The propagation of a single dominant crack has been considered in the applications. In the case of fragmentation, with multiple cracks propagating simultaneously, or crack branching, other methods in which cohesive cracks can propagate along the cohesive interfaces already interposed between all adjacent elements would result more effective (see, e.g. [3,6,8]).

A number of possible future developments is listed below.

- A simple linear softening mixed-mode cohesive model has been used for the considered implementation. Incorporating other cohesive models into the proposed framework could provide more accurate results in the case of complex material behavior.
- The proposed simulation strategy has been tested only in a 2D framework. The extension to 3D with the use of polyhedral VES does not present difficulties from the formulation point of view, while some complications have to be expected for the geometrical treatment of the propagating fracture planes, which generate new VEs.
- When a self-stabilized VE is crossed by a crack, its number of edges is increased, and the VE may require the stabilization illustrated in this work. It could be worth considering the possibility to obtain another self-stabilized VE by projecting the displacement field onto a higher-order polynomial strain model. In view of the heterogeneity of the strain model across elements, this would also require to reconsider the smoothing strategy adopted to estimate the stress state at the fictitious crack tip.

## CRediT authorship contribution statement

**Y. Chen:** Writing – review & editing, Writing – original draft, Validation, Software, Investigation, Methodology. **D. Sun:** Writing – review & editing, Visualization, Software, Formal analysis, Investigation. **Q. Li:** Writing – review & editing, Supervision, Funding acquisition. **U. Perego:** Writing – review & editing, Writing – original draft, Supervision, Funding acquisition, Conceptualization, Formal analysis.

## Declaration of competing interest

The authors declare that they have no known competing financial interests or personal relationships that could have appeared to influence the work reported in this paper.

## Acknowledgments

U. Perego gratefully acknowledges the financial support of the Ministry of University and Research (MUR) through project PRIN2022-PNRR P2022BH5CB, CUP D53D23018840001: UE funding – NextGenerationEU – mission 4, component 2, investment 1.1. Q. Li was supported by the National Natural Science Foundation of China (Nos. 12172270), Qin Chuangyuan 'Scientists + Engineers' Team Construction Project in Shaanxi Province (2022KXJ-085). Y. Chen was supported by the China Scholarship Council (Nos. 202106280007).

## Data availability

Data will be made available on request.

## References

[1] J.C. Simo, J. Oliver, F. Armero, An analysis of strong discontinuities induced by strain-softening in rate-independent inelastic solids, Comput. Mech. 12 (5) (1993) 277–296, http://dx.doi.org/10.1007/BF00372173/METRICS.
[2] B. Bourdin, G. Francfort, J.-J. Marigo, The variational approach to fracture, J. Elasticity 91 (1–3) (2008) 5–148, http://dx.doi.org/10.1007/s10659-007-9107-3.
[3] A. Pandolfi, B. Li, M. Ortiz, Modeling fracture by material-point erosion, Int. J. Fract. 184 (1–2) (2013) 3–16, http://dx.doi.org/10.1007/s10704-012-9788-x.
[4] A. Pandolfi, K. Weinberg, M. Ortiz, A comparative accuracy and convergence study of eigenerosion and phase-field models of fracture, Comput. Methods Appl. Mech. Engrg. 386 (2021) 114078, http://dx.doi.org/10.1016/J.CMA.2021.114078.
[5] X.P. Xu, A. Needleman, Numerical simulations of fast crack growth in brittle solids, J. Mech. Phys. Solids 42 (9) (1994) 1397–1434, http://dx.doi.org/10.1016/0022-5096(94)90003-5.
[6] G.T. Camacho, M. Ortiz, Computational modelling of impact damage in brittle materials, Int. J. Solids Struct. 33 (1996) 2899–2938, http://dx.doi.org/10.1016/0020-7683(95)00255-3.
[7] M. Ortiz, A. Pandolfi, Finite-deformation irreversible cohesive elements for three-dimensional crack-propagation analysis, Internat. J. Numer. Methods Engrg. 44 (9) (1999) 1267–1282, http://dx.doi.org/10.1002/(SICI)1097-0207(19990330)44:9<1267::AID-NME486>3.0.CO;2-7.
[8] R. Radovitzky, A. Seagraves, M. Tupek, L. Noels, A scalable 3D fracture and fragmentation algorithm based on a hybrid, discontinuous Galerkin, cohesive element method, Comput. Methods Appl. Mech. Engrg. 200 (2011) 326–344, http://dx.doi.org/10.1016/j.cma.2010.08.014.
[9] V.P. Nguyen, Discontinuous Galerkin/extrinsic cohesive zone modeling: Implementation caveats and applications in computational fracture mechanics, Eng. Fract. Mech. 128 (2014) 37–68, http://dx.doi.org/10.1016/j.engfracmech.2014.07.003.

[10] S.C. Aduloju, T.J. Truster, A variational multiscale discontinuous Galerkin formulation for both implicit and explicit dynamic modeling of interfacial fracture, Comput. Methods Appl. Mech. Engrg. 343 (2019) 602–630, http://dx.doi.org/10.1016/j.cma.2018.08.025.
[11] S.E. Leon, D.W. Spring, G.H. Paulino, Reduction in mesh bias for dynamic fracture using adaptive splitting of polygonal finite elements, Internat. J. Numer. Methods Engrg. 100 (8) (2014) 555–576, http://dx.doi.org/10.1002/nme.4744.
[12] P. Bocca, A. Carpinteri, S. Valente, Mixed mode fracture of concrete, Int. J. Solids Struct. 27 (9) (1991) 1139–1153, http://dx.doi.org/10.1016/0020-7683(91)90115-V.
[13] V.M. Nguyen-Thanh, X. Zhuang, H. Nguyen-Xuan, T. Rabczuk, P. Wriggers, A virtual element method for 2D linear elastic fracture analysis, Comput. Methods Appl. Mech. Engrg. 340 (2018) 366–395, http://dx.doi.org/10.1016/J.CMA.2018.05.021.
[14] N. Moës, J. Dolbow, T. Belytschko, A finite element method for crack growth without remeshing, Internat. J. Numer. Methods Engrg. 46 (1) (1999) 131–150, http://dx.doi.org/10.1002/(SICI)1097-0207(19990910)46:1<131::AID-NME726>3.0.CO;2-J.
[15] L. Beirão da Veiga, F. Brezzi, A. Cangiani, G. Manzini, L.D. Marini, A. Russo, Basic principles of virtual element methods, Math. Models Methods Appl. Sci. 23 (01) (2013) 199–214, http://dx.doi.org/10.1142/S0218202512500492.
[16] L. Beirão da Veiga, F. Brezzi, L.D. Marini, Virtual elements for linear elasticity problems, SIAM J. Numer. Anal. 51 (2) (2013) 794–812, http://dx.doi.org/10.1137/120874746.
[17] M.F. Benedetto, A. Borio, S. Scialò, Mixed virtual elements for discrete fracture network simulations, Finite Elem. Anal. Des. 134 (2017) 55–67, http://dx.doi.org/10.1016/J.FINEL.2017.05.011.
[18] F. Aldakheel, B. Hudobivnik, A. Hussein, P. Wriggers, Phase-field modeling of brittle fracture using an efficient virtual element scheme, Comput. Methods Appl. Mech. Engrg. 341 (2018) 443–466, http://dx.doi.org/10.1016/J.CMA.2018.07.008.
[19] F. Aldakheel, B. Hudobivnik, P. Wriggers, Virtual element formulation for phase-field modeling of ductile fracture, Int. J. Multiscale Comput. Eng. 17 (2) (2019) 181–200, http://dx.doi.org/10.1615/IntJMultCompEng.2018026804.
[20] A. Hussein, F. Aldakheel, B. Hudobivnik, P. Wriggers, P.-A. Guidault, O. Allix, A computational framework for brittle crack-propagation based on efficient virtual element method, Finite Elem. Anal. Des. 159 (2019) 15–32, http://dx.doi.org/10.1016/J.FINEL.2019.03.001.
[21] E. Benvenuti, A. Chiozzi, G. Manzini, N. Sukumar, Extended virtual element method for two-dimensional linear elastic fracture, Comput. Methods Appl. Mech. Engrg. 390 (2022) 114352, http://dx.doi.org/10.1016/J.CMA.2021.114352.
[22] Y. Chen, D. Sun, U. Perego, Q. Li, Brittle crack propagation simulation based on virtual element method and $J_k$-integral fracture criterion, Eng. Fract. Mech. to appear (2024).
[23] E. Artioli, S. Marfia, E. Sacco, VEM-based tracking algorithm for cohesive/frictional 2D fracture, Comput. Methods Appl. Mech. Engrg. 365 (2020) 112956, http://dx.doi.org/10.1016/j.cma.2020.112956.
[24] S. Marfia, E. Monaldo, E. Sacco, Cohesive fracture evolution within virtual element method, Eng. Fract. Mech. 269 (2022) 108464, http://dx.doi.org/10.1016/j.engfracmech.2022.108464.
[25] H. Choi, H. Chi, K. Park, Virtual element method for mixed-mode cohesive fracture simulation with element split and domain integral, Int. J. Fract. 240 (1) (2023) 51–70, http://dx.doi.org/10.1007/S10704-022-00675-7/FIGURES/22.
[26] S. Mariani, U. Perego, Extended finite element method for quasi-brittle fracture, Internat. J. Numer. Methods Engrg. 58 (1) (2003) 103–126, http://dx.doi.org/10.1002/nme.761.
[27] M.F. Benedetto, A. Caggiano, G. Etse, Virtual elements and zero thickness interface-based approach for fracture analysis of heterogeneous materials, Comput. Methods Appl. Mech. Engrg. 338 (2018) 41–67, http://dx.doi.org/10.1016/J.CMA.2018.04.001.
[28] R. Dimitri, M. Trullo, L.D. Lorenzis, G. Zavarise, Coupled cohesive zone models for mixed-mode fracture: A comparative study, Eng. Fract. Mech. 148 (2015) 145–179, http://dx.doi.org/10.1016/j.engfracmech.2015.09.029.
[29] F. Confalonieri, U. Perego, A new framework for the formulation and validation of cohesive mixed-mode delamination models, Int. J. Solids Struct. 164 (2019) 168–190, http://dx.doi.org/10.1016/J.IJSOLSTR.2018.12.032.
[30] A.M. D'Altri, S. de Miranda, L. Patruno, E. Sacco, An enhanced VEM formulation for plane elasticity, Comput. Methods Appl. Mech. Engrg. 376 (2021) 113663, http://dx.doi.org/10.1016/j.cma.2020.113663.
[31] A. Chen, N. Sukumar, Stabilization-free serendipity virtual element method for plane elasticity, Comput. Methods Appl. Mech. Engrg. 404 (2023) 115784, http://dx.doi.org/10.1016/J.CMA.2022.115784, arXiv:2202.10037.
[32] A. Lamperti, M. Cremonesi, U. Perego, A. Russo, C. Lovadina, A Hu–Washizu variational approach to self-stabilized virtual elements: 2D linear elastostatics, Comput. Mech. 71 (5) (2023) 935–955, http://dx.doi.org/10.1007/s00466-023-02282-2.
[33] B.-B. Xu, F. Peng, P. Wriggers, Stabilization-free virtual element method for finite strain applications, Comput. Methods Appl. Mech. Engrg. 417 (2023) 116555, http://dx.doi.org/10.1016/j.cma.2023.116555.
[34] S. Berrone, A. Borio, F. Marcon, A stabilization-free virtual element method based on divergence-free projections, Comput. Methods Appl. Mech. Engrg. 424 (2024) 116885, http://dx.doi.org/10.1016/J.CMA.2024.116885.
[35] A. Borio, C. Lovadina, F. Marcon, M. Visinoni, A lowest order stabilization-free mixed virtual element method, Comput. Math. Appl. 160 (2024) 161–170, http://dx.doi.org/10.1016/J.CAMWA.2024.02.024.
[36] M. Cremonesi, A. Lamperti, C. Lovadina, U. Perego, A. Russo, Analysis of a stabilization-free quadrilateral virtual element for 2d linear elasticity in the Hu-Washizu formulation, Comput. Math. Appl. 155 (2024) 142–149, http://dx.doi.org/10.1016/j.camwa.2023.12.001.
[37] S. Berrone, A. Borio, F. Marcon, Lowest order stabilization free virtual element method for the Poisson equation, 2021, http://dx.doi.org/10.48550/arXiv.2103.16896, arXiv preprint arXiv:2103.16896.
[38] K. Park, H. Chi, G.H. Paulino, On nonconvex meshes for elastodynamics using virtual element methods with explicit time integration, Comput. Methods Appl. Mech. Engrg. 356 (2019) 669–684, http://dx.doi.org/10.1016/J.CMA.2019.06.031.
[39] E. Denarié, V.E. Saouma, A. Iocco, D. Varelas, Concrete fracture process zone characterization with fiber optics, J. Eng. Mech. 127 (5) (2001) 494–502, http://dx.doi.org/10.1061/(ASCE)0733-9399(2001)127:5(494).
[40] T. Gerasimov, L. De Lorenzis, On penalization in variational phase-field models of brittle fracture, Comput. Methods Appl. Mech. Engrg. 354 (2019) 990–1026, http://dx.doi.org/10.1016/j.cma.2019.05.038.
[41] B. Winkler, Traglastuntersuchungen von unbewehrten und bew. Betonstrukturen auf der Grundlage eines objektiven Werkstoffgesetzes für Beton (Ph.D. thesis), Ph. D. thesis, University of Innsbruck, Austria, 2001.
[42] T. Most, C. Bucher, Energy-based simulation of concrete cracking using an improved mixed-mode cohesive crack model within a meshless discretization, Int. J. Numer. Anal. Methods Geomech. 31 (2) (2007) p.285–305, http://dx.doi.org/10.1002/NAG.536.
[43] Y.S. Jenq, S.P. Shah, Mixed-mode fracture of concrete, Int. J. Fract. 38 (2) (1988) 123–142, http://dx.doi.org/10.1007/BF00033002.